J. Fluid Mech. (2009), *vol.* 641, *pp.* 263–296. © Cambridge University Press 2009
doi:10.1017/S0022112009991662

Dynamics of strain-hardening and strain-softening capsules in strong planar extensional flows via an interfacial spectral boundary element algorithm for elastic membranes

W. R. DODSON III[1] AND P. DIMITRAKOPOULOS[2]†

[1]Fischell Department of Bioengineering, University of Maryland, College Park, MD 20742, USA

[2]Department of Chemical and Biomolecular Engineering, University of Maryland, College Park, MD 20742, USA

(Received 16 May 2008; revised 31 July 2009; accepted 12 August 2009; first published online 25 November 2009)

In the present study we investigate the dynamics of initially spherical capsules (made from elastic membranes obeying the strain-hardening Skalak or the strain-softening neo-Hookean law) in strong planar extensional flows via numerical computations. To achieve this, we develop a three-dimensional spectral boundary element algorithm for membranes with shearing and area-dilatation tensions in Stokes flow. The main attraction of this approach is that it exploits all the benefits of the spectral methods (i.e. high accuracy and numerical stability) but without creating denser systems. To achieve continuity of the interfacial geometry and its derivatives at the edges of the spectral elements during the interfacial deformation, a membrane-based interfacial smoothing is developed, via a Hermitian-like interpolation, for both the interfacial shape and the membrane elastic forces. Our numerical results show that no critical flow rate exists for both Skalak and neo-Hookean capsules in the moderate and strong planar extension flows considered in the present study. As the flow rate increases, both capsules reach elongated ellipsoidal steady-state configurations; the cross-section of the Skalak capsule preserves its elliptical shape, while the neo-Hookean capsule becomes more and more lamellar. The curvature at the pointed edges of these elongated steady-state shapes shows a very fast increase with the flow rate. The large interfacial deformations are accompanied with the development of strong membrane tensions especially for the strain-hardening Skalak capsule; the computed increase of the membrane tensions with the flow rate or the shape extension can be used to predict rupture of a specific membrane (with known lytic tension) due to excessive tensions. The type of the experiment imposed on the capsule as well as the applied flow rate affect dramatically the time evolution of the capsule edges owing to the interaction of the hydrodynamic forces with the membrane tensions; when a spherical Skalak capsule is let to deform in a strong flow, very large edge curvatures (with respect to the steady-state value) are developed during the transient evolution.

Key words: capsule/cell dynamics, interfacial flows (free surface), low-Reynolds-number flows

---

† Email address for correspondence: dimitrak@umd.edu

1. Introduction

The study of the interfacial dynamics of artificial or physiological capsules (i.e. membrane-enclosed fluid volumes) in Stokes flow has seen an increased interest during the last few decades due to their numerous engineering and biomedical applications. Artificial capsules have wide applications in the pharmaceutical, food and cosmetic industries (Pozrikidis 2003). In pharmaceutical processes, for example, capsules are commonly used for the transport of medical agents. In addition, the motion of red blood cells through vascular microvessels has long been recognized as a fundamental problem in physiology and biomechanics, since the main function of these cells, to exchange oxygen and carbon dioxide with the tissues, occurs in capillaries (Baskurt & Meiselman 2003; Popel & Johnson 2005).

In this work we restrict our interest to elastic membranes with shearing and area-dilatation resistance but negligible bending resistance. This class represents a wide range of artificial capsules. Experimental findings for biocompatible alginate capsules (Carin *et al.* 2003), synthetic polysiloxane (Husmann *et al.* 2005) and aminomethacrylate capsules (Pieper, Rehage & Barthès-Biesel 1998) compare very well with theoretical models that ignore bending resistance. Therefore, several earlier theoretical investigations have focused on this class of problems (e.g. Pozrikidis 1995; Ramanujan & Pozrikidis 1998; Secomb, Hsu & Pries 1998; Lac *et al.* 2004; Lac & Barthès-Biesel 2005). To a great extent, this model also applies to the human red blood cells, where the interior haemoglobin solution is enclosed by a multi-layer membrane whose reduced bending modulus (with respect to its shearing resistance) is $O(10^{-3})$ (Mohandas & Chasis 1993; Secomb *et al.* 1998).

To solve this problem, several theoretical methodologies have been employed. Secomb and co-workers (Secomb *et al.* 1998; Secomb, Hsu & Pries 2001, 2002) utilized lubrication approximation to solve for the axisymmetric cell deformation in a capillary and investigated the effects of non-uniform vessel diameter and the presence of a flow-resistive layer on the vessel wall. Eggleton & Popel (1998) employed an immersed boundary method to study the capsule deformation in shear flows, for different initial capsule shapes (i.e. spherical, oblate and biconcave discoid shapes) and for small to moderate capillary numbers over relatively short time periods. Recently, Doddi & Bagchi (2008) employed an immersed boundary/front-tracking method to study the effects of inertia on the hydrodynamic interactions between two liquid capsules in simple shear flow. In addition, several computational methods based on the boundary integral formulation have been developed. The main benefit of this approach is the reduction of the problem dimensionality by one owing to the fact that only the system's surface needs to be discretized. The simplest boundary integral methods have assumed axisymmetry which further reduces the problem dimensionality (e.g. Diaz, Pelekasis & Barthès-Biesel 2000; Kwak & Pozrikidis 2001). Fully three-dimensional boundary integral methods have also been developed based on structured or unstructured mesh discretization of the capsule interface (e.g. Pozrikidis 1995; Navot 1998; Ramanujan & Pozrikidis 1998; Lac *et al.* 2004; Lac & Barthès-Biesel 2005). We emphasize that all previously implemented numerical methods are based on low-order interpolation schemes.

It is of interest to note that the results of the existing three-dimensional methodologies agree well at moderate flow rates (where the interfacial deformation is not very large). In this range of flow rates, the numerical findings are also in agreement with experimental observations (Eggleton & Popel 1998; Lac *et al.* 2004) and thus provide physical insight on the capsule dynamics at moderate deformations.

However, current understanding of capsule dynamics at high flow rates is rather limited, even though such flows are commonly encountered in industrial and physiological processes. For example, for millimetre-size capsules made from aminomethacrylate membranes with shearing modulus $G_s = O(10^{-2})\,\mathrm{N\,m^{-1}}$, flow rates $Ca = O(1)$ require shear stress $\mu G = O(10)\,\mathrm{Pa}$ (Pieper *et al.* 1998). (The definition of these variables are provided later in § 2.) Experimental studies on capsule deformation in linear flow fields are still very limited in number and restricted to moderate deformations (e.g. Chang & Olbricht 1993*a*,*b*), even though the required flow rates for large capsule deformation have long been achieved in corresponding experiments with droplets and bubbles (e.g. Bentley & Leal 1986; Ha & Leal 2001). The asymptotic solutions for initially spherical capsules by Barthès-Biesel and co-workers are restricted to small deformations (Barthès-Biesel 1980; Barthès-Biesel & Rallison 1981; Barthès-Biesel & Sgaier 1985). The state-of-the-art (low-order) three-dimensional computational methodologies are unable to find stable steady-state capsule shapes at high flow rates. These methodologies either predict interfacial breaking even at moderate flow rates (Pozrikidis 1995; Lac *et al.* 2004) or are restricted to moderate interfacial deformations (Eggleton & Popel 1998; Ramanujan & Pozrikidis 1998; Doddi & Bagchi 2008). The failure at large deformations of the existing theoretical studies points to the fact that the dynamic behaviour of a membrane-like interface submerged in an ambient flow is a complicated physical problem due to the coupling of the fluid dynamics with the (nonlinear) elastic mechanics of the membrane.

The present paper has thus two main goals: (*a*) to develop a robust methodology for the efficient and accurate determination of complicated capsule shapes in Stokes flows and (*b*) to investigate the dynamics of two types of membranes, strain-hardening and strain-softening, in strong planar extensional flows.

In § 3, we develop an interfacial spectral boundary element (SBE) algorithm for membranes with shearing and area-dilatation tensions. The main attraction of our high-order algorithm is that it combines the benefits of the spectral methods, including high accuracy and numerical stability as the number of discretization points increases, with the geometric versatility associated with boundary element schemes. In addition, our methodology is not affected by the disadvantage of the spectral methods used with partial differential equations, namely the requirement to deal with dense systems, because in boundary integral formulations the resulting systems are always dense, independent of the form of the discretization (Muldowney & Higdon 1995; Dimitrakopoulos & Higdon 1998; Wang & Dimitrakopoulos 2006). Our method also exploits all the benefits of the boundary element techniques, i.e. reduction of the problem dimensionality and great parallel scalability.

In § 4, we present the major characteristic of our interfacial algorithm, i.e. its high accuracy in determining both the geometric properties of a given shape (such as the interfacial curvature) and the dynamic evolution of the capsule's shape. The transient dynamics of both strain-hardening Skalak and strain-softening neo-Hookean capsules in a planar extensional flow are investigated in § 5, while in § 6 we consider the steady-state properties for these capsules, including the evolution of the interfacial shape and the membrane tensions with the flow rate and the capsule extension. In contrast to earlier low-order methodologies which predict interfacial breaking at strong enough flows (and thus the existence of a critical flow rate), our spectral algorithm predicts stable transient and steady-state capsule shapes. As the flow rate increases, both capsules reach elongated ellipsoidal steady-state configurations, but the neo-Hookean shapes are thinner and flatter (i.e. more lamellar) than the Skalak ones for the same extension. The pointed profiles of these shapes are in qualitative agreement with experimental findings (Barthès-Biesel 1991) and suggest a very fast increase of the edge curvature with the flow rate. An extended summary of our results is included in § 7.

2. Mathematical formulation

2.1. *Fluid dynamics*

We consider a three-dimensional capsule with an elastic interface in an infinite ambient fluid. The interior (fluid 1) and exterior (fluid 2) are Newtonian, with viscosities $\lambda\mu$ and μ and the same density. The capsule size is specified by its volume V or equivalently by the radius a of a sphere of volume $4\pi a^3/3 = V$. Far away, the flow approaches the undisturbed flow $\boldsymbol{u}^{\infty}$, e.g. a planar extensional flow $\boldsymbol{u}^{\infty} = G\,(x, -y, 0)$ or a simple shear flow $\boldsymbol{u}^{\infty} = G\,(z, 0, 0)$, where G is the shear rate. In this study, the characteristic length a is used as the length scale, while the time is scaled with the flow time scale G^{-1}.

Assuming low-Reynolds-number flows, the governing equations in fluid 2 are the Stokes equations and continuity,

$$\nabla \cdot \boldsymbol{\sigma} = -\nabla p + \mu \nabla^2 \boldsymbol{u} = 0, \tag{1}$$

$$\nabla \cdot \boldsymbol{u} = 0, \tag{2}$$

while inside the capsule, the same equations apply with the viscosity replaced by $\lambda\mu$.

At the interface, the velocity is continuous, and we define the surface stress vector (or hydrostatic traction) $\Delta \boldsymbol{f}$ from the stress tensor $\boldsymbol{\sigma}$ and the surface unit normal $\boldsymbol{n}$, i.e.

$$\boldsymbol{u}_1 = \boldsymbol{u}_2 = \boldsymbol{u}, \tag{3}$$

$$\Delta \boldsymbol{f} \equiv \boldsymbol{n} \cdot (\boldsymbol{\sigma}_2 - \boldsymbol{\sigma}_1). \tag{4}$$

Here the subscripts designate quantities evaluated in fluids 1 and 2, respectively, while $\boldsymbol{n}$ is the unit normal which we choose to point into fluid 2.

Based on the standard boundary integral formulation, for a freely suspended capsule, the velocity at a point $\boldsymbol{x}_0$ on the interface S_B may be determined by the following boundary integral equation:

$$(1+\lambda)\boldsymbol{u}(\boldsymbol{x}_0) - 2\boldsymbol{u}^{\infty}(\boldsymbol{x}_0) = -\frac{1}{4\pi\mu}\int_{S_B} [\boldsymbol{S} \cdot \Delta \boldsymbol{f} - (1-\lambda)\mu \boldsymbol{T} \cdot \boldsymbol{u} \cdot \boldsymbol{n}](\boldsymbol{x})\, \mathrm{d}S, \tag{5}$$

where the tensors $\boldsymbol{S}$ and $\boldsymbol{T}$ are the fundamental solutions for the velocity and stress for the three-dimensional Stokes equations, respectively (e.g. Pozrikidis 2001; Lac *et al.* 2004; Dimitrakopoulos 2007).

Owing to the no-slip condition at the interface, the time evolution of the material points of the membrane may be determined via the kinematic condition at the interface,

$$\frac{\partial \boldsymbol{x}}{\partial t} = \boldsymbol{u}. \tag{6}$$

To produce a closed system of equations, the surface stress $\Delta \boldsymbol{f}$ is determined by the membrane dynamics as described in the following subsection.

2.2. *Membrane dynamics*

Our description of the membrane dynamics is based on the well-established continuum approach and the theory of thin shells (Barthès-Biesel & Rallison 1981; Gould 1999;

Pozrikidis 2003; Lac *et al.* 2004). Typical membrane thickness ranges from $O(\mu\text{m})$ for alginate capsules (Carin *et al.* 2003) to $O(\text{nm})$ for synthetic polysiloxane capsules (Husmann *et al.* 2005) (i.e. it is several orders of magnitude smaller than the size of the capsule), and thus the thin-shell theory has proven to be an excellent description of these membranes (Pieper *et al.* 1998; Carin *et al.* 2003; Pozrikidis 2003; Husmann *et al.* 2005). We emphasize that the study of capsules or cells via the continuum approach and the theory of thin shells is now a rather classical problem. Thus in this section we present a laconic description of the membrane statics; more details may be found in relevant review papers and books (Pozrikidis 2001, 2003).

Let the membrane be a two-dimensional surface, with arbitrary curvilinear coordinates θ^α. We define the complete basis system consisting of the surface tangents $\boldsymbol{t}_\alpha$ and the unit normal $\boldsymbol{n}$ by

$$\boldsymbol{t}_\alpha = \frac{\partial \boldsymbol{x}}{\partial \theta^\alpha}, \qquad \boldsymbol{n} = \frac{\boldsymbol{t}_1 \times \boldsymbol{t}_2}{|\boldsymbol{t}_1 \times \boldsymbol{t}_2|}. \tag{7}$$

A set of reciprocal tangents $\boldsymbol{t}^\beta$ can be defined such that $\boldsymbol{t}_\alpha \boldsymbol{\cdot} \boldsymbol{t}^\beta = \delta_\alpha{}^\beta$. (Note that $\boldsymbol{n}$ is its own reciprocal.) Tensors can then be expressed in either covariant or contravariant components with respect to the base in the standard manner (Papastavridis 1999). Note that in this work the Greek indices range over 1 and 2, while Einstein notation is employed for (every two) repeated indices.

Tensors defined in $\mathscr{R}^3$ must then be transformed into $\mathscr{R}^2$. The stress tensor $\boldsymbol{\sigma}$ is integrated across the solid phase to produce the second-order tensor $\boldsymbol{\tau}$, which contains in-plane resultants, and into the first-order tensor (vector) $\boldsymbol{q}$, which contains transverse shearing forces (Barthès-Biesel & Rallison 1981; Pozrikidis 2003). We will assume that there is no resistance to flexure, in which case $\boldsymbol{q} = 0$ and $\boldsymbol{\tau}$ is symmetric.

A force balance over an arbitrary differential area of membrane shows that $\Delta \boldsymbol{f} = -\nabla_s \boldsymbol{\cdot} \boldsymbol{\tau}$ (Waxman 1984; Pozrikidis 2001, 2003), which in contravariant form gives

$$\Delta \boldsymbol{f} = -(\tau^{\alpha\beta}|_\alpha \, \boldsymbol{t}_\beta + b_{\alpha\beta} \, \tau^{\alpha\beta} \, \boldsymbol{n}). \tag{8}$$

In this expression, $b_{\alpha\beta}$ is the surface curvature tensor and the $\tau^{\alpha\beta}|_\alpha$ notation denotes covariant differentiation. (See Papastavridis 1999 for further explication of the calculus of differential surface geometry.)

The in-plane stress resultant tensor $\boldsymbol{\tau}$ is the two-dimensional analogue of the three-dimensional stress, but to describe elastic behaviour it is also necessary to have an analogue of strain. This is accomplished by projection of the three-dimensional deformation gradient $\boldsymbol{F}$, which transforms elements from a reference object into a deformed state. Denoting the deformed element $\mathrm{d}\boldsymbol{x}$ and the reference element $\mathrm{d}\boldsymbol{X}$, $\mathrm{d}\boldsymbol{x} = \boldsymbol{F} \boldsymbol{\cdot} \mathrm{d}\boldsymbol{X}$ (Barthès-Biesel & Rallison 1981; Lubarda 2002). (For vectors, capital letters denote the reference shape, and lower-case letters the deformed shape; e.g. the reference tangents and normal will be denoted $\boldsymbol{T}_\alpha$ and $\boldsymbol{N}$, respectively.) The surface strain tensor is derived by the projection

$$\boldsymbol{A} \equiv (\boldsymbol{I} - \boldsymbol{nn}) \boldsymbol{\cdot} \boldsymbol{F} \boldsymbol{\cdot} (\boldsymbol{I} - \boldsymbol{NN}). \tag{9}$$

The effect of the projection is that the linear operator $\boldsymbol{A}$ only transforms elements from the plane of the reference surface, and it only transforms those elements into the plane of the deformed surface. The strain tensor $\boldsymbol{A}$ is calculated efficiently by $\boldsymbol{A} = \boldsymbol{t}_\alpha \boldsymbol{T}^\alpha$ (Steigmann & Ogden 1999).

The left Cauchy–Green strain tensor $\boldsymbol{V}^2 = \boldsymbol{A} \boldsymbol{\cdot} \boldsymbol{A}^T$ has two non-zero eigenvalues, corresponding to the squares of the principal stretch ratios λ_α. The corresponding unit eigenvectors $\hat{\boldsymbol{b}}_\alpha$ are the directions of principal stretch. The in-plane stress tensor

$\boldsymbol{\tau}$ is given by the dyadic product (Lubarda 2002),

$$\boldsymbol{\tau} = \sum_{\alpha} \tau_{\alpha}^{P} \hat{\boldsymbol{b}}_{\alpha} \hat{\boldsymbol{b}}_{\alpha}. \tag{10}$$

The principal elastic tensions τ_{α}^{P} are calculated from the stretch ratios via a constitutive law which depends on the material composition of the membrane (Barthès-Biesel, Diaz & Dhenin 2002; Pozrikidis 2003). The material law of Skalak *et al.* (1973) describing certain biological capsules (such as red blood cells) as well as membranes obtained by interfacial polymerization is given by

$$\tau_1^P = \frac{G_s \lambda_1}{\lambda_2} \left(\lambda_1^2 - 1 + C\lambda_2^2[(\lambda_1\lambda_2)^2 - 1]\right). \tag{11}$$

(To calculate τ_2^P, reverse the λ_α subscripts.) In the equation above, G_s is the shearing modulus, while the dimensionless parameter C is associated with the area-dilatation resistance of the membrane. The Mooney–Rivlin law is intended to represent a thin, incompressible elastic sheet such as polymeric materials,

$$\tau_1^P = \frac{G_s}{\lambda_1 \lambda_2} \left(\lambda_1^2 - \frac{1}{\lambda_1^2 \lambda_2^2}\right) \left[\Psi + \lambda_2^2(1 - \Psi)\right], \tag{12}$$

where the parameter Ψ varies in the range [0, 1]. Here, local area dilatation correlates with membrane thickness. In the special case in which $\Psi = 1$, the Mooney–Rivlin law simplifies to the neo-Hookean form

$$\tau_1^P = \frac{G_s}{\lambda_1 \lambda_2} \left(\lambda_1^2 - \frac{1}{\lambda_1^2 \lambda_2^2}\right). \tag{13}$$

Note that the membrane mechanics involves two moduli, one for shearing and one for area dilatation. The parameter C which is associated with area dilatation is already dimensionless. The shearing modulus G_s can also be used to form a dimensionless group when the membrane is in contact with an ambient flow. The associated (elastic) capillary number

$$Ca = \frac{\mu G a}{G_s} \tag{14}$$

shows the ratio of viscous flow forces to resistive elastic forces on the membrane. (Here μ is the viscosity of the ambient fluid, G the shear rate and a the capsule's characteristic length scale.) Note that slightly different dimensionless groups have been used in earlier studies (e.g. Navot 1998; Ramanujan & Pozrikidis 1998). In this study, the reported membrane tensions are scaled with G_s.

3. Interfacial spectral boundary element (SBE) algorithm

3.1. *Spectral boundary element (SBE) discretization*

The numerical solution of the boundary integral equations described previously in §2 is achieved through an extension of the SBE method which originally was developed for Stokes flow computations with fixed boundaries (Muldowney & Higdon 1995) and later was extended to interfacial dynamics of fluid droplets (Dimitrakopoulos & Higdon 1998; Wang & Dimitrakopoulos 2006; Dimitrakopoulos 2007; Dimitrakopoulos & Wang 2007). Here we present a concise description of the SBE method; more details may be found in the aforementioned references.

The discretization used in the SBE method is a block-structured mesh in which the initial capsule surface is divided into $N_E \geqslant 6$ curvilinear quadrilateral elements.

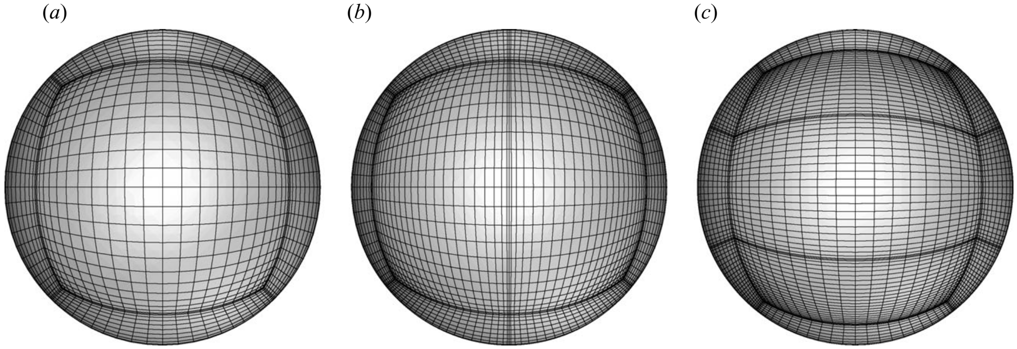

FIGURE 1. SBE discretization of a spherical capsule into (a) $N_E = 6$ elements based on cube projection, (b) $N_E = 10$ elements based on division into two rows of elements along the x-direction and (c) $N_E = 14$ elements based on division into three rows of elements along the y-direction.

Since we employ quadrilateral elements, a convenient way of discretizing the initial interface is via prism projection; e.g. the capsule surface is projected on to a cube or parallelepiped whose faces correspond to the interfacial elements as shown in figure 1(*a*). We also have the ability to subdivide the prism's faces into additional spectral elements as shown in figure 1(*b, c*). By partitioning the surface in this way, we can control the distribution of spectral points on the surface to maximize efficiency and accuracy. In addition, calculations via interpolation are more efficient, since they are based on the spectral points defined on each element (and not on the entire interface).

Each quadrilateral surface element is then mapped on to a square parametric domain $[-1, 1]^2$. The geometric variables on each element are discretized using Lagrangian interpolation in terms of the parametric variables ξ, η on the square domain, e.g.

$$\boldsymbol{x}(\xi, \eta) = \sum_{i=1}^{N_B} \sum_{j=1}^{N_B} \boldsymbol{x}(\xi_i, \eta_j)\, h_i(\xi)\, h_j(\eta), \tag{15}$$

where h_i is the $(N_B - 1)$-order Lagrangian interpolant polynomial. The physical variables $\boldsymbol{u}$ and $\boldsymbol{f}$ are represented similarly. The base points (ξ_i, η_j) for the interpolation are chosen as the zeros of N_B-order orthogonal polynomials; this yields the spectral convergence associated with the orthogonal polynomial expansions.

The boundary integral equations (5) admit two different types of points. The collocation points $\boldsymbol{x}_0$ of the left-hand side where the equation is required to hold and the basis points $\boldsymbol{x}$ of the right-hand side where the physical variables $\boldsymbol{u}$ and $\boldsymbol{f}$ are defined. The spectral element method as implemented here employs collocation points of Gauss quadrature, i.e. in the interior of the element only. (As a result the boundary integral equation holds even for singular elements where the normal vector is not uniquely defined, e.g. for a membrane attached to a solid surface, similar to our earlier studies on attached droplets; Dimitrakopoulos & Higdon 1998.) In addition, we use basis points of Gauss–Lobatto quadrature (i.e. in the interior and the edges of the elements; Canuto *et al.* 1998), which facilitate the interfacial smoothing described in § 3.2. The numerical integration associated with (5) is performed by Gauss–Legendre quadrature with the aid of variable transformations. Owing to the singularity in the kernels, special care must be taken to ensure the accurate numerical evaluation of these integrations as described in Muldowney & Higdon (1995).

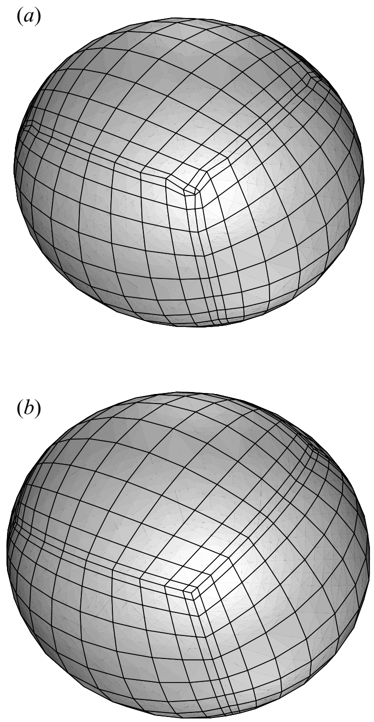

FIGURE 2. (*a*) Interfacial shape of a Skalak capsule with $C = 1$ and $\lambda = 1$ in a planar extensional flow with $Ca = 0.35$ at time $t = 0.123$. A fourth-order Runge–Kutta scheme with zero-order (i.e. geometry) continuity at the edges of adjacent elements was employed with $N_E = 6$, $N_B = 12$ and $\Delta t = 10^{-3}$. For this specific case, the disparities in the derivatives of the geometry near the elements corners cause interfacial breaking at the next time step. (*b*) As in (*a*), but now our first-order capsule interfacial smoothing is employed at every time step. The capsule interface is continuous and smooth across the spectral elements at all times as our results up to $t = 10$ (i.e. well past steady state) indicate.

3.2. *Membrane interfacial smoothing*

To determine the capsule's shape as a function of time, the kinematic condition (6) is applied based on a high-order explicit scheme (usually the fourth-order Runge–Kutta method). We emphasize that in the present work, the grid points represent material points of the capsule's interface, and thus both normal and tangential velocity components must be employed. This differs from the case of droplets, where the grid points commonly represent interfacial marker points (Ramanujan & Pozrikidis 1998; Wang & Dimitrakopoulos 2006).

The explicit time integration is applied at the (Gauss–Lobatto) basis points $\boldsymbol{x}$ where the interfacial velocity $\boldsymbol{u}$ is determined. Similar to the drop dynamics, the time step Δt should be sufficiently small to ensure numerical stability, i.e.

$$\Delta t < O(Ca\,\Delta x_{min}), \tag{16}$$

where Δx_{min} is the minimum length scale appearing in the computational problem, e.g. the minimum grid spacing (Pozrikidis 2001; Wang & Dimitrakopoulos 2006).

If we apply the advancing scheme described above, requiring coincidence of the end points belonging to adjacent elements and without any additional geometric constraints, the resulting algorithm is unstable as shown in figure 2(*a*) for a Skalak capsule in a planar extensional flow. The numerical instability is caused by the discontinuity of interfacial derivatives at the edges of the spectral elements as shown in this figure. In particular, starting from a smooth interfacial shape, the geometry derived by the time integration of (6) shows discrepancies at its derivatives at the edges of the spectral elements. These discrepancies are very small after one time step; in particular they are several orders of magnitude smaller than the accuracy of the numerical method. (For the case shown in figure 2, the accuracy of the numerical method is at least three significant digits, while the derivative discrepancies are $O(10^{-8})$ or smaller.) However, if these discrepancies are left unattended, local errors build over time, resulting in severe derivative disparities between coincident points on adjacent elements. This instability first manifests as interfacial tips located at the element corners as shown in figure 2(a) and quickly causes failure of the numerical method.

We emphasize that these derivative disparities across the spectral elements result from the (spectral) element nature of our algorithm and the fact that we use Gauss–Lobatto coincidence (i.e. zero-order geometric continuity) across the elements. Similar disparities appear for droplet deformation as discussed in Wang & Dimitrakopoulos (2006). To avoid the resulting numerical instabilities additional interfacial smoothing is necessary.

Wang & Dimitrakopoulos (2006) developed a first-order smoothing scheme (i.e. continuity of up to the first derivative of the interfacial geometry) for drop dynamics which is based on averaging, at the end of each time step, of the local tangent vectors belonging to consecutive spectral elements. When we apply the droplet smoothing algorithm to capsules, we find that the resulting algorithm is numerically unstable due to discrepancies very similar to those shown in figure 2(a). The reason for this instability lies in the fact that the smoothing scheme of Wang & Dimitrakopoulos (2006) is valid for interfacial marker points such as those used for droplet dynamics. For the material points of a capsule, the smoothing causes the grid points to drift on the surface which, owing to the mapping with the reference shape, creates non-existent local strains and finally instability.

With this in mind, we have developed a first-order smoothing scheme for capsule deformation that preserves the correspondence between the reference shape and the current deformed geometry. Our smoothing methodology for capsule dynamics includes smoothing, at the end of each time step, of the transient interfacial shape as well as of the surface stress forces which depend on the membrane material.

To describe the interfacial smoothing of the capsule shape, let the non-smoothed interfacial shape of the Gauss–Lobatto basis points at time $t + \Delta t$, derived by the time integration of (6), be identified as $\boldsymbol{x}^{old}$. The first step is to average the position of all coincident points of adjacent spectral elements. For coincident nodes belonging to adjacent elements [1] and [2], the new position is

$$\boldsymbol{x}^{new}_{[1]} = \boldsymbol{x}^{new}_{[2]} = \frac{1}{2}\left(\boldsymbol{x}^{old}_{[1]} + \boldsymbol{x}^{old}_{[2]}\right). \tag{17}$$

This achieves zero-order (i.e. position) continuity across the interface as well as high-order continuity (i.e. continuity of the geometric derivatives) along the local direction parallel to the element edges (see figure 2b).

Thus, to achieve complete first-order continuity on the surface, we need to smooth in the other interfacial direction. For this, we employ a tensor quantity as the basis for our first-order smoothing, i.e. the surface strain tensor $\boldsymbol{A} = \boldsymbol{t}_\alpha \boldsymbol{T}^\alpha$ which incorporates the reference shape. We average this tensor over coincident nodes, e.g.

$$\boldsymbol{A}^{new} = \frac{1}{2}\left[(\boldsymbol{t}_\alpha \boldsymbol{T}^\alpha)^{old}_{[1]} + (\boldsymbol{t}_\alpha \boldsymbol{T}^\alpha)^{old}_{[2]}\right]. \tag{18}$$

Note that because the reference shape is time invariant, it always has high-order continuity across the elements; e.g. the reference tangents $\boldsymbol{T}_\alpha$ are always continuous at the elements' edges. We then use $(\boldsymbol{A})^{new}$ to obtain a new partial surface derivative in the direction away from the element boundary, i.e.

$$\left(\frac{\partial \boldsymbol{x}}{\partial \theta^\alpha}\right)^{new} = (\boldsymbol{t}_\alpha)^{new} = (\boldsymbol{A})^{new} \cdot \boldsymbol{T}_\alpha. \tag{19}$$

The final step of our first-order geometry smoothing scheme is to generate the updated geometry at the time step $t + \Delta t$ which preserves zero-order continuity and in addition incorporates the new derivative values at the coincident points. To achieve this goal, we employ the two-dimensional Hermitian interpolation presented in Wang & Dimitrakopoulos (2006), which utilizes function and first derivative values at the end points but only function values at the interior points of a spectral element (see § IV in Wang & Dimitrakopoulos 2006).

In addition, we smooth the surface force vector $\Delta \boldsymbol{f}$ (which is determined by the membrane properties as discussed in § 2.2) via a similar first-order smoothing which applies before we utilize $\Delta \boldsymbol{f}$ in the boundary integral system, i.e. at the beginning of each time step. This smoothing mirrors the geometric smoothing, except that the interpolated function is $\Delta \boldsymbol{f}$ instead of $\boldsymbol{x}$. In particular, we first achieve zero-order continuity by averaging $\Delta \boldsymbol{f}$ across coincident points. The tensor used for the subsequent first-order smoothing is the surface gradient

$$\nabla_S(\Delta \boldsymbol{f}) = \boldsymbol{t}^\alpha \frac{\partial(\Delta \boldsymbol{f})}{\partial \theta^\alpha}. \tag{20}$$

Then we average $\nabla_S(\Delta \boldsymbol{f})$ at coincident points and recover the new derivatives by

$$\left(\frac{\partial(\Delta \boldsymbol{f})}{\partial \theta^\alpha}\right)^{new} = \boldsymbol{t}_\alpha \cdot (\nabla_S(\Delta \boldsymbol{f}))^{new}. \tag{21}$$

Afterwards, we perform the two-dimensional Hermitian interpolation as with the interfacial geometry described previously.

In figure 2(*b*) we show the time evolution of the capsule presented earlier in figure 2(*a*), but now we employ our first-order smoothing scheme for capsules at every time step. In contrast to the earlier result, the new smoothing scheme suppresses numerical instability for elastic capsule deformation at all times, i.e. well past steady state.

As a closure to this section, we emphasize that the membrane smoothing methodology we have developed in this paper is an efficient technique to preserve the continuity of the interfacial spectral geometry and its derivatives for membrane-like interfaces. Our first-order smoothing, which we employ at every time step, is able to achieve this, since the discrepancies at the edges of the spectral elements are very small when treated at the end of each time step. The entire process, including the relevant two-dimensional Hermitian interpolation, requires a computational cost of only $O(N_E\, N_B)$, i.e. $O(N_B)$ on each spectral element, owing to the fact that it is implemented through products of one-dimensional rules. (The reduction of the operation cost is a characteristic feature of all product rules in spectral methods; Canuto *et al.* 1998.)

4. Properties of capsule interfacial algorithm

We have conducted numerous tests to verify the correctness, accuracy and robustness of our interfacial algorithm for capsules with elastic tensions. We have investigated the deformation of initially spherical capsules with several viscosity ratios in steady linear flows (i.e. simple shear and planar extensional flows), while we have considered all material laws mentioned in § 2.2. To quantify the interfacial deformation over time we monitor the capsule's length L, width S and depth W, as well as Taylor's deformation parameter

$$D = \frac{L - S}{L + S}. \tag{22}$$

The capsule dimensions are determined as the semi-axes of the ellipsoid which has the same inertia tensor as that of the capsule (Ramanujan & Pozrikidis 1998; Lac *et al.* 2004).

Our computational results presented in this paper were mainly derived by employing $N_E = 6, 10, 14$ spectral elements (based on different element divisions of the capsule surface) with $N_B = 10$–14 basis points. For the time integration, we usually employed the fourth-order Runge–Kutta scheme with time step in the range $\Delta t = 10^{-4}$–10^{-3}. The accuracy of our results was verified by employing smaller time steps and different grid densities for several representative cases.

In particular, for the transient and steady-state dynamics of Skalak and neo-Hookean capsules in moderate and strong planar extensional flows presented in §§ 5 and 6, we mainly employed two different element divisions of the capsule surface. We divided the interfacial shape into two rows of elements along the x-direction or three rows of elements along the y-direction as shown in figure 1. Both element divisions preserve the three symmetry planes of the extensional flow; our algorithm exploits these symmetries to reduce the computational cost (Dimitrakopoulos & Higdon 1998; Dimitrakopoulos 2007). Convergence runs covering the entire interfacial evolution (i.e. well past steady state) with $N_B = 10$–14 basis points showed that our results for the interfacial shape presented in §§ 5 and 6 are accurate to at least three significant digits for both moderate and high flow rates except for the very highest flow rates at which the interfacial shape was determined with an accuracy of at least two significant digits. More details on the accuracy of our results are included in the captions of figures 5, 10 and 11 in § 5.

In addition, for moderate flow rates we have compared our transient and steady-state results with published results in shear and planar extensional flows from several low-order methods (e.g. Eggleton & Popel 1998; Ramanujan & Pozrikidis 1998; Lac *et al.* 2004) by printing our results in the same scale as the earlier results and superimposing them. All reported comparisons have revealed that the curves are nearly coincident and thus within the expected near-1 % error of the earlier low-order methodologies. Additional comparisons have been made with the actual data of Lac *et al.* (2004). For example, for a Skalak capsule with $C = 1$ in a planar extensional flow with $Ca = 0.45, 0.6$, Lac *et al.* (2004) found a steady-state deformation $D = 0.549, 0.6$ and length $L = 1.78, 1.95$, while according to our computations $D = 0.548, 0.595$ and $L = 1.76, 1.90$. In the case of a neo-Hookean capsule in a planar extensional flow with $Ca = 0.18, 0.21$, Lac *et al.* (2004) found at steady state $D = 0.504, 0.552$ and $L = 1.62, 1.73$, while according to our computations $D = 0.507, 0.552$ and $L = 1.60, 1.71$.

It is of interest to note that in strong flows, the surface area of specific spectral elements may show a significant increase. As mentioned earlier, convergence runs have verified the accuracy of our results. We note that the spectral boundary method for fixed surfaces has proven to be very accurate even when it employs large spectral elements (e.g. see § 5 in Muldowney & Higdon 1995). As discussed in our earlier publications for droplets (Wang & Dimitrakopoulos 2006; Dimitrakopoulos 2007) and also found in the present study for capsules, our spectral method is able to determine accurately the interfacial geometry at large deformations when the spectral grid evolves reasonably over time, i.e. when it is not very distorted. With respect to this issue, interfacial dynamics of capsules is computationally more efficient than that for droplets, since in the former case the spectral grid represents the material points of a membrane, and thus it is not severely distorted over time as shown in all the three-dimensional shapes presented in this paper.

During the entire interfacial deformation, our computations show that the capsule volume is usually preserved to at least seven significant digits, while for the very highest flow rates reported in this paper, the capsule volume is accurate to at least five significant digits. In our earlier study with droplets (Wang & Dimitrakopoulos 2006) and the present study with capsules, we also have the option to adjust the volume of the capsule at the end of each time step (e.g. after the application of the smoothing methodology) by

$$\boldsymbol{x}^{new} - \boldsymbol{x}_c = \sqrt[3]{\frac{V_0}{V}}\,(\boldsymbol{x} - \boldsymbol{x}_c), \tag{23}$$

where $\boldsymbol{x}$, $\boldsymbol{x}_c$ and V are the interfacial shape, the volume centroid and the volume of the capsule, respectively, at the end of each time step while V_0 is the initial capsule volume. For the problems studied in this work, both ways produce identical results.

Having established the validity and robustness of our interfacial algorithm with the representative examples mentioned above, we proceed now to discuss its spectral performance. In particular, a major property of our interfacial algorithm is its high accuracy with increasing the number of discretization points which results from the spectral nature of our algorithm. We emphasize that the high accuracy of our methodology holds for both the geometric properties of a given shape, such as the interfacial curvature, and the dynamic evolution of the capsule's shape.

Figure 3 shows the maximum absolute error in the computed curvature as the number of spectral points N increases from 150 to 3750 for a spherical capsule and two representative lamellar capsules. (As discussed in § 5, strain-softening capsules obtain lamellar shapes at strong extensional flows.) We note the exponential convergence of our spectral algorithm is in direct contrast to the common linear or quadratic convergence associated with low-order algorithms.

The spectral accuracy also holds for the determination of the evolution of any interfacial property. To show this, we calculated the transient evolution of an initially spherical capsule for a moderate and a large capillary number, i.e. $Ca = 0.35, 1.5$. In both cases, we kept the number of elements N_E fixed and increased the number of basis points in the range $N_B = 6$–15. Our results for $N_B = 15$ were regarded as a close approximation for the exact answer. Figure 4 shows the relative error in the computed deformation D as the number of spectral points $N = N_E\, N_B^2$ increases. The exponential convergence shown for our results for $Ca = 0.35$ represents the time $t = 0.15$ where $D \approx 0.14$ while the capsule length has been increased by 15 %. For $Ca = 1.5$, our results represent the time $t = 0.60$ where $D \approx 0.49$ and the capsule length has been increased by 71 %. In this case the convergence is not as fast as for $Ca = 0.35$ because we employed a rather coarse grid to describe a quite deformed

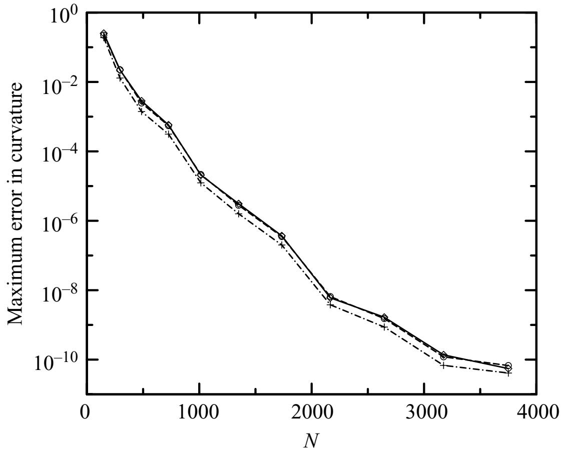

FIGURE 3. Maximum absolute error in the computed curvature versus the number of spectral points $N = N_E\, N_B^2$ for a sphere (——) and different lamellar ellipsoids: - - - -, $a = 2, b = 1, c = 0.5$; $-\cdot-$, $a = 4, b = 1, c = 0.25$ (where a, b and c are the semi-axes of the ellipsoids). The exponential convergence shown in this figure was generated by employing $N_E = 6$ spectral elements and varying the number of basis points N_B from 5 to 25. The exact value was used to determine the numerical error.

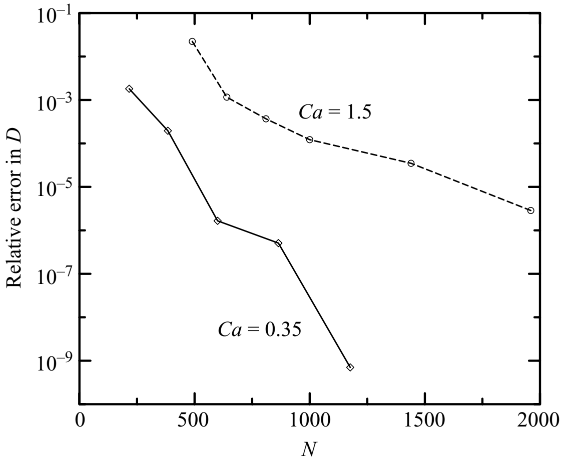

FIGURE 4. Relative error in the computed deformation D versus the number of spectral points $N = N_E\, N_B^2$ for a Skalak capsule with $C = 1$ and $\lambda = 1$ in a planar extensional flow with $Ca = 0.35, 1.5$. For the case $Ca = 0.35$, our results represent the time $t = 0.15$ where $D \approx 0.14$ while the capsule length has been increased by 15 % and its width has been decreased by 13 %. For $Ca = 1.5$, our results represent the time $t = 0.60$ where $D \approx 0.49$ while the capsule length has been increased by 71 % and its width has been decreased by 41 %. Our results were generated by employing $N_E = 6$ spectral elements for $Ca = 0.35$ and $N_E = 10$ elements for $Ca = 1.5$ and varying the number of basis points N_B from 6 to 15. In both cases, the results for $N_B = 15$ were used to determine the numerical error.

interfacial shape; however, our spectral method is able to achieve a relative error of 2×10^{-6} by employing $N_E = 10$ and $N_B = 14$, i.e. with only $N = 1960$ spectral points.

It is of interest to note that the accuracy in determining the interfacial shape during transient dynamics shown in figure 4 also represents the accuracy of our spectral method for steady-state shapes of similar deformation, since in our computations the accuracy is restricted by the space discretization (and not the time step).

The observed high accuracy of our present membrane algorithm is similar to the one we found for drop dynamics (Wang & Dimitrakopoulos 2006; Dimitrakopoulos 2007). We emphasize that the difference in the interfacial accuracy between our spectral algorithms and low-order methods is dramatic, since the latter commonly achieve only linear convergence by increasing the number of the employed grid points.

5. Transient dynamics of Skalak and neo-Hookean capsules in a planar extensional flow

In this section we consider the transient dynamics of an initially spherical capsule with $\lambda = 1$ in a planar extensional flow $\boldsymbol{u}^{\infty} = G\,(x, -y, 0)$ for moderate and large capillary numbers. We study both strain-hardening Skalak capsules with $C = 1$ and strain-softening neo-Hookean capsules. The main goal of this section is to investigate the physical behaviour of elastic capsules, including the evolution of the interfacial shape and the membrane tensions, at large deformations, where current understanding of capsule dynamics is rather limited, as discussed in § 1.

In particular, earlier computational studies based on low-order methodologies in shear or extensional flows either found that there exists a critical flow rate above which the capsule's interface cannot reach a steady state and thus breaks (Pozrikidis 1995; Lac *et al.* 2004) or were restricted to rather moderate steady-state deformations (Eggleton & Popel 1998; Ramanujan & Pozrikidis 1998; Doddi & Bagchi 2008). For planar extensional flows, the recent comprehensive work of Lac *et al.* (2004) found that steady-state shapes exist only for a region of moderate capillary numbers $[Ca_L, Ca_H]$. For a Skalak capsule with $C = 1$, $Ca_L = 0.15$ and $0.6 < Ca_H < 0.75$, while for a neo-Hookean capsule $Ca_L = 0.14$ and $0.21 < Ca_H < 0.24$. The corresponding maximum steady-state deformations were reported to be $D = 0.53$ and $D \approx 0.57$ for the two types of membranes (see table 1 in Lac *et al.* 2004). Above these flow rates Ca_H, the authors found that the capsule develops high-curvature tips and that the deformation and membrane tensions increase without bound, causing interfacial breaking.

We note that our computational results agree with those of Lac *et al.* (2004) for low flow rates; i.e. for capillary numbers $Ca < Ca_L$ compressive tensions result in wrinkling around the capsule equator which causes interfacial breaking near steady state. However, our findings at high flow rates are dramatically different from those of the earlier study.

Thus in this section we will try to address the following questions: (i) Does a critical flow rate exist or not for capsule dynamics? (ii) If no critical flow rate exists, what is the capsule's configuration and dynamics at strong flow rates? (iii) How does the behaviour of strain-hardening capsules differ from that of strain-softening ones?

Figure 5 shows the deformation of a Skalak capsule in a planar extensional flow for several capillary numbers. As Ca increases, the capsule's length L is increased while its width S is decreased as shown in figure 5(b); this results in a monotonic increase of the capsule's deformation D at steady state with the capillary number as illustrated in figure 5(a). We note that the surface area of the capsule (not presented here) shows a monotonic increase with time and the flow rate (similar to that of the capsule's length L). A careful examination of figure 5(a, b) reveals that while the capsule's width S reaches steady state at about the same time for all the flow rates (or Ca) studied here, it takes more time for the capsule's length L (and thus for its deformation D)

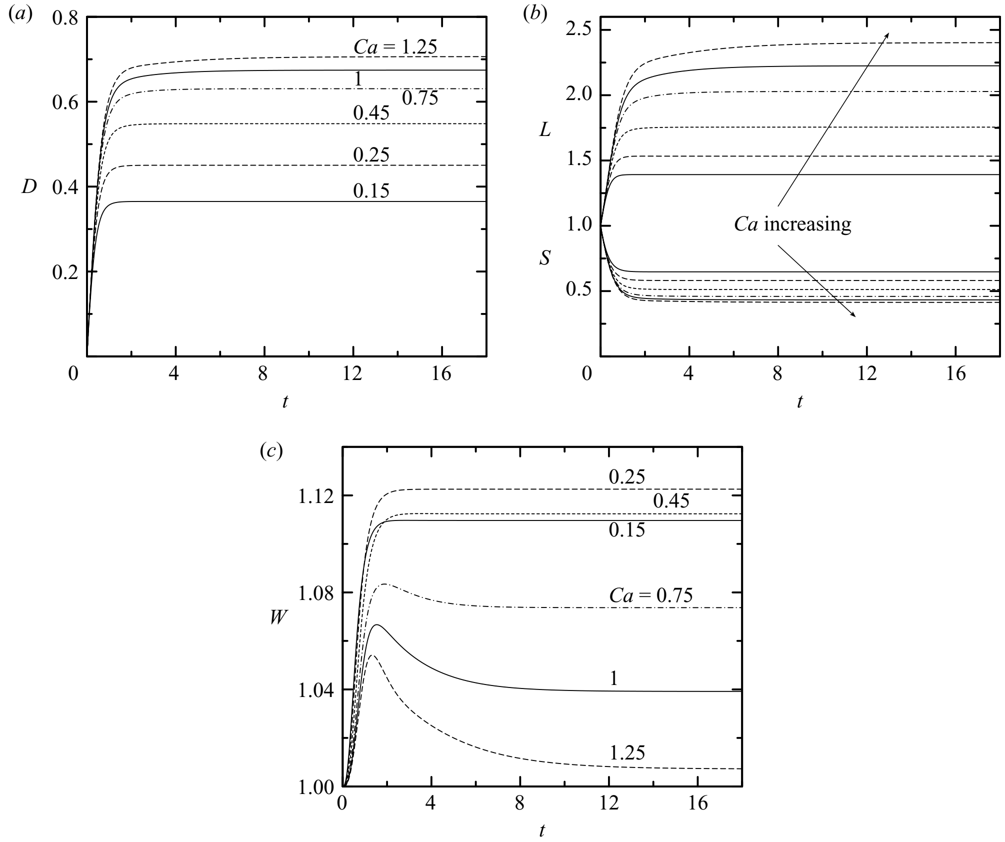

FIGURE 5. Evolution of a Skalak capsule with $C = 1$ and $\lambda = 1$ in a planar extensional flow for capillary number $Ca = 0.15, 0.25, 0.45, 0.75, 1, 1.25$. Time evolution of (*a*) the capsule's deformation D, (*b*) its length L and width S and (*c*) its depth W. (Note that for $Ca = 0.75, 1$ our computations cover the time period [0, 20], while for $Ca = 1.25$ they cover the period [0, 30].) Our convergence runs revealed that our results are accurate to at least three significant digits, and thus if we include the different convergence runs on the same plot, they show no difference.

to reach steady state for the high capillary numbers, $Ca = 0.75, 1, 1.25$. (This is the reason that for these flow rates we monitor the capsule evolution for a long time period; in particular, for $Ca = 0.75, 1$ our computations cover the time period [0, 20], while for $Ca = 1.25$ they cover the period [0, 30].)

To explain this anisotropy, in figure 5(*c*) we present the evolution of the capsule's depth W for the same capillary numbers. At low flow rates (e.g. $Ca = 0.15, 0.25, 0.45$), the capsule's depth W shows a monotonic increase with time, reaching steady state at about the same time as the other two dimensions of the capsule. (Observe that W shows a maximum with the capillary number even in this range of flow rates.) However, the time evolution of the capsule's depth W is quite different at the large flow rates $Ca = 0.75, 1, 1.25$; after a fast initial growth, W decreases over time, while at steady state the higher capillary number corresponds to smaller depth. This non-trivial behaviour of the capsule's depth W affects mostly its length L; i.e. the late-time reduction of the depth W at high flow rates causes a further increase of its length L as shown in figure 5(*a*).

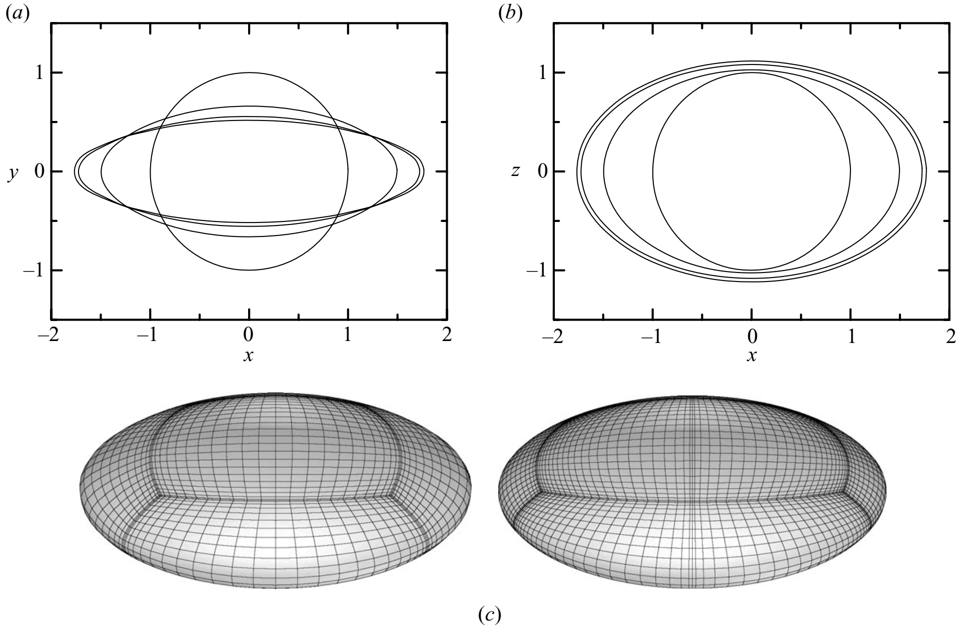

FIGURE 6. Evolution of a Skalak capsule with $C=1$ and $\lambda=1$ in a planar extensional flow with $Ca=0.45$. (*a*) Capsule profile (i.e. interface intersection) with the plane $z=0$ at times $t=0, 0.5, 1, 18$. (*b*) Capsule profile (i.e. interface intersection) with the plane $y=0$ at times $t=0, 0.5, 1, 18$. (*c*) Capsule shape (computed based on two different element divisions employing $N_B=6, 10$ spectral elements) at time $t=18$, i.e. well past steady state.

The evolution of the capsule's profile in the $z=0$ and $y=0$ planes for $Ca=0.45$ is shown in figure 6(*a, b*). As the capsule deforms, the increase of its length L along with the corresponding decrease of its width S, shown in figure 5(*b*), results in a rather elongated shape in the $z=0$ plane as depicted in figure 6(*a*). However, at the same time the capsule's depth W is slightly increased as shown in figures 5(*c*) and 6(*b*). Both actions result in a flat ellipsoidal shape of the capsule at steady state as seen in figure 6(*c*). (Note that the three-dimensional views of the capsule shape presented in this section were derived from the actual spectral grid by spectrally interpolating to $N_B=25$.)

We emphasize that our results for the evolution of the capsule's deformation D for the moderate capillary number $Ca=0.45$ shown in figure 5(*a*) are in very good agreement with the computations of Lac *et al.* (2004) reported in their figure 16. In addition, the capsule profile in the plane $z=0$ at steady state shown in figure 6(*a*) is in very good agreement with that from the study of Lac *et al.* (2004) reported in their figure 17.

Thus, our results agree with those of Lac *et al.* (2004) in their region of stability (i.e. for moderate capillary numbers); however, our spectral boundary interfacial algorithm also predicts stable steady-state shapes for higher capillary numbers, e.g. $Ca \geqslant 0.75$. We emphasize that our computational investigation at these large flow rates covers an extended time period (up to time $t=30$ for $Ca=1.25$) to verify the validity of our results.

To provide more information on the behaviour of the capsule at large capillary numbers, in figure 7 we present our numerical results for $Ca=1.25$. As seen in figure 7(*a, b*), over time the capsule elongates in the x-direction and thins in the y-direction, while its depth shows a rather small but non-trivial variation (which was presented earlier in figure 5*c*). The capsule shape at steady state is shown in figure 7(*c*).

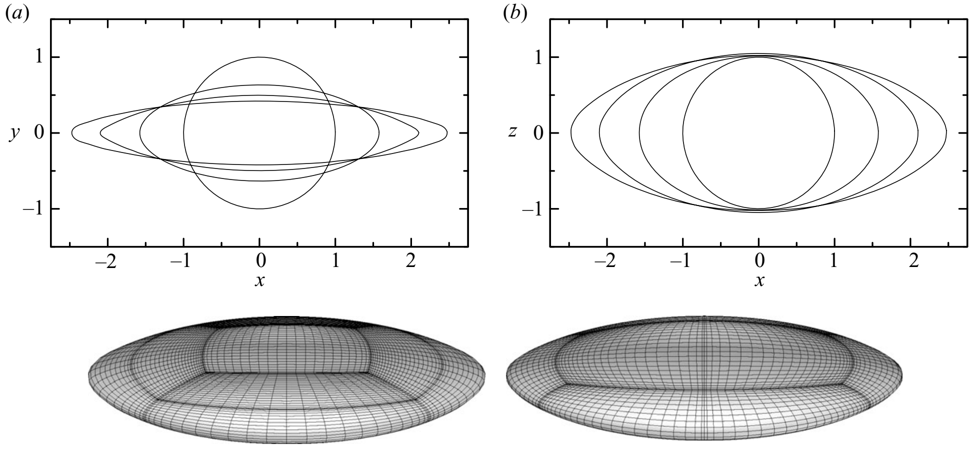

(c)

FIGURE 7. Evolution of a Skalak capsule with $C = 1$ and $\lambda = 1$ in a planar extensional flow with $Ca = 1.25$. (a) Capsule profile (i.e. interface intersection) with the plane $z = 0$ at times $t = 0, 0.5, 1, 30$. (b) As in (a) but for the capsule profile with the plane $y = 0$. (c) Capsule shape (computed based on two different element divisions employing $N_B = 14, 10$ spectral elements) at time $t = 30$, i.e. well past steady state.

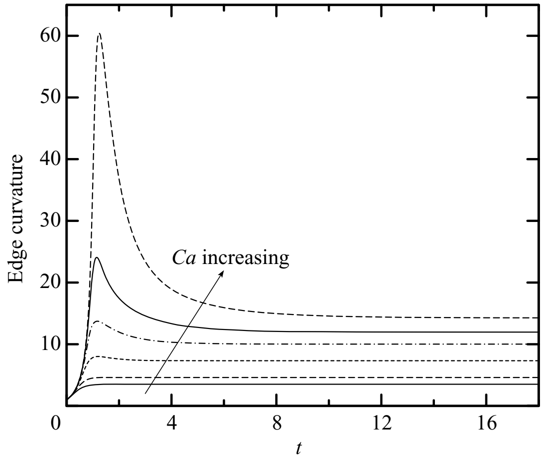

FIGURE 8. Time evolution of the edge curvature (determined along the interfacial cross-section with the $z = 0$ plane) for a Skalak capsule with $C = 1$ and $\lambda = 1$ in a planar extensional flow with $Ca = 0.15, 0.25, 0.45, 0.75, 1, 1.25$.

It is of interest to observe that the capsule profile with the plane $z = 0$, shown in figure 7(a), becomes quite pointed around time $t = 1$, while at steady state the edges in the x-direction are more rounded but still more pointed than those for $Ca = 0.45$ shown in figure 6(a). This non-monotonic behaviour for the capsule edges is not observed at moderate flow rates at which the edges become monotonically more pointed with time up to steady state, as shown in figure 6(a).

To investigate this issue more, in figure 8 we plot the time evolution of the edge curvature for several flow rates. This figure clearly supports our observations based on the evolution of the capsule profiles. In particular, for moderate flow rates

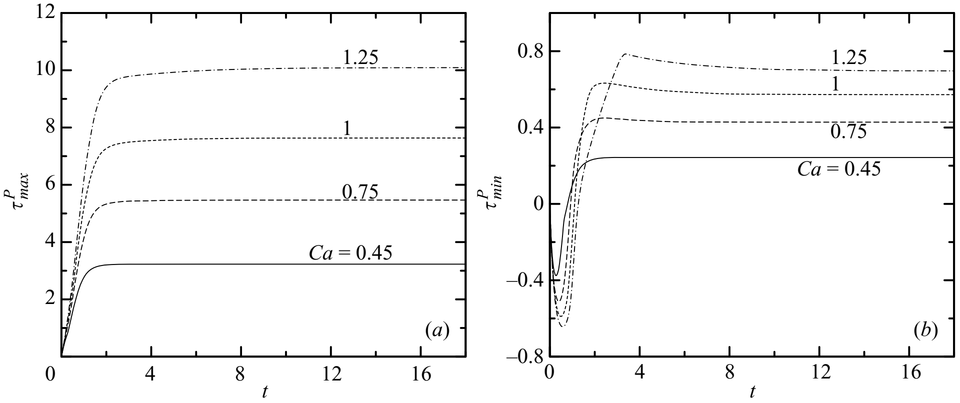

FIGURE 9. Time evolution of the (*a*) maximum τ^P_{max} and (*b*) minimum τ^P_{min} principal tensions among the spectral discretization points on the membrane for a Skalak capsule with $C = 1$ and $\lambda = 1$ in a planar extensional flow with $Ca = 0.45, 0.75, 1, 1.25$.

$Ca = 0.15, 0.25, 0.45$ the edge curvature shows a monotonic increase over time up to steady state. On the other hand, its evolution for high flow rates $Ca = 0.75, 1, 1.25$ is dramatically different especially for the highest flow rate. At strong flows, the edge curvature shows a fast initial increase followed by a similarly fast decrease towards steady state where higher flow rates result in greater edge curvature, i.e. more pointed edges. We emphasize that the maximum value of the edge curvature during the transient evolution can be several times its steady-state value as clearly shown for $Ca = 1.25$; thus it is during the (initial) transient evolution where the capsule edges become very pointed. In addition, note that our first-order smoothing does not affect the tip curvature, since the capsule edges fall in the interior of the two edge elements as shown in figure 7(*c*).

To investigate the membrane dynamics, in figure 9 we present the time evolution of the maximum τ^P_{max} and minimum τ^P_{min} principal tensions over the capsule surface for several capillary numbers. (Note that in our study the reported membrane tensions are scaled with G_s.) As shown in figure 9(*a*), the maximum principal tension increases with time from a zero initial value until steady state, and thus it is always positive. In addition, higher capillary numbers cause larger values of τ^P_{max} at steady state. The evolution of the minimum principal tension is more complicated. Starting from zero, τ^P_{min} decreases with time, and thus it obtains a negative value at early times. Later the minimum tension increases with time and becomes positive. Since the membrane tensions at steady state are everywhere positive (i.e. the tensions are tensile), no compression is developed, and thus the pointed edges of the Skalak capsule are concave for the flow rates studied in this paper, as seen in figures 6 and 7.

The location of the minimum and maximum tensions on the capsule surface follows the same basic trend for the different capillary numbers. Initially, the minimum tension τ^P_{min} occurs at the capsule edges; e.g. looking at the capsule profiles in figure 7, the minimum tension is located at the intersection of the capsule's surface with the x-axis. After an initial transient period, however, the location of the surface minimum changes. The new surface minimum occurs at the capsule largest depth, i.e. at the intersection of the capsule's surface with the z-axis. The direction of this tension at late times has no x-component; i.e. this tension acts entirely in the yz cross-section. The maximum tension τ^P_{max} is initially located at the largest width of the capsule, e.g.

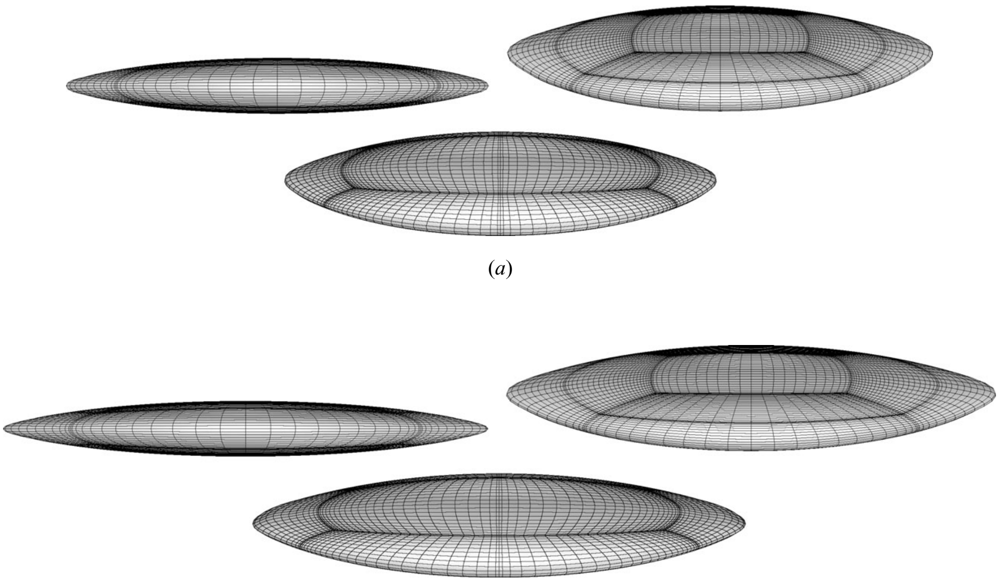

(*a*)

(*b*)

FIGURE 10. Steady-state shapes for a Skalak capsule with $C = 1$ and $\lambda = 1$ in a planar extensional flow with (*a*) $Ca = 2$ and (*b*) $Ca = 2.5$. The three-dimensional views of the capsule shown were determined based on two different element divisions employing $N_B = 14$, 10 spectral elements. Our convergence runs revealed that for both capillary numbers the interfacial shape was determined with a maximum relative error of 5×10^{-3}.

at the points $x = z = 0$. After a transient period, this tension switches location and is located in the same place as the steady-state minimum tension; thus at steady state the locations of the minimum and maximum tensions become congruent. Note that the maximum tension τ^P_{max} always points in the direction of the capsule's elongation.

Proceeding further, we determine the steady-state shape of the Skalak capsule at much higher flow rates by gradually increasing the capillary number (with step size $\Delta Ca = 0.25, 0.5$) and allowing the system to reach steady state after each flow rate increase. Our spectral algorithm is able to determine accurately these very elongated steady-state configurations as shown in figure 10 for capillary number $Ca = 2, 2.5$.

It is of interest to note that during the gradual increase of the flow rate (where the capsule is let to reach steady state after each flow rate increase), the edge curvature shows a monotonic increase with time even in these strong flow rates. This contracts the evolution of the capsule edges observed in figure 8, where a spherical capsule is let to deform in a steady strong flow.

To explain the edge evolution in these two types of experiments, we need to consider the interaction of the hydrodynamic forces with the membrane tensions. When a spherical capsule is let to deform in a steady flow, the restoring membrane tensions are initially weak (owing to the small interfacial deformation) but increase over time as the capsule deforms. In a moderate flow rate, the deforming hydrodynamic forces are also weak, and thus the capsule edges become monotonically more pointed over time as shown in figure 8 for $Ca = 0.15, 0.25, 0.45$. On the other hand, shortly after a spherical capsule is let to deform in a strong flow, the strong hydrodynamic forces overcome the weak membrane tensions; thus the edge curvature increases, trying to balance the hydrodynamic forces, as suggested by (8), and initially the capsule tips

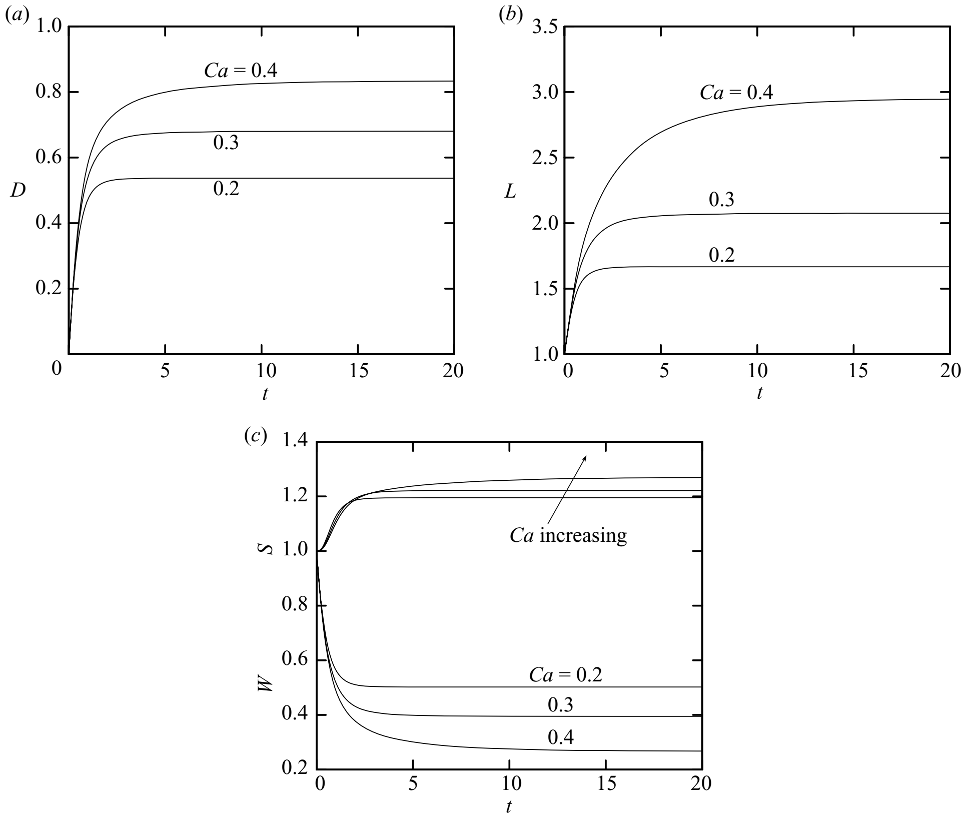

FIGURE 11. Evolution of a neo-Hookean capsule with $\lambda = 1$ in a planar extensional flow for capillary number $Ca = 0.2, 0.3, 0.4$. Time evolution of (*a*) the capsule's deformation D, (*b*) its length L and (*c*) its width S and depth W. (Note that for $Ca = 0.4$ our computations cover the time period $[0, 40]$.) Our convergence runs revealed that for $Ca = 0.4$ our results show a maximum relative error of 7×10^{-3}, while for $Ca = 0.2, 0.3$ our results are accurate to at least three significant digits.

become very pointed (as shown in figure 8 for $Ca = 0.75, 1, 1.25$). In this case, after some time the membrane tensions increase and cause a decrease of the edge curvature towards its steady-state value. It is of interest to note that for these high flow rates, the capsule tension τ^P_{max} reaches its maximum value at about the same time as the capsule deformation D, i.e. at time $t \approx 1.5$–2; the fast decrease of the edge curvature also starts at about this time (see figures 5*a*, 8 and 9*a*). In the second type of experiment, i.e. via a gradual increase of the flow rate, the gradual capsule deformation is accompanied by a gradual increase of the membrane tensions, and thus the capsule edges become monotonically more pointed over time.

We now turn our attention to strain-softening membranes and investigate the dynamics of a neo-Hookean capsule in a planar extensional flow. Figure 11 shows the evolution towards steady state of the capsule's deformation and lengths for several capillary numbers, i.e. $Ca = 0.2, 0.3, 0.4$. We note that for $Ca = 0.4$ we have continued our computations until $t = 40$ (not shown here) to ensure that a steady state has been reached. This figure reveals that the evolution of the neo-Hookean capsule is monotonic over time and thus not so complicated as the Skalak capsule. For the soft-straining membrane, the capsule's length L and depth W increase with time, while its width S decreases until steady state is reached; this results in a monotonic increase of

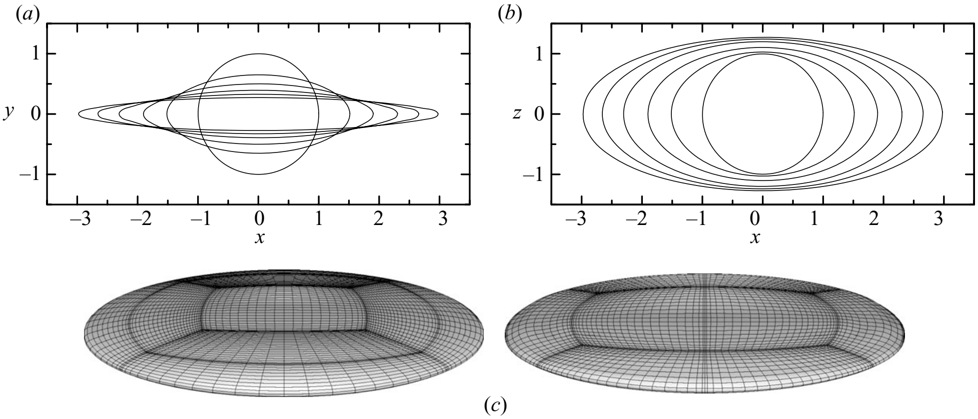

FIGURE 12. Evolution of a neo-Hookean capsule with $\lambda = 1$ in a planar extensional flow with $Ca = 0.4$. (*a*) Capsule profile (i.e. interface intersection) with the plane $z = 0$ at times $t = 0, 0.5, 1, 2, 4, 40$. (*b*) As in (*a*) but for the capsule profile with the plane $y = 0$. (*c*) Capsule shape (based on two different element divisions) at time $t = 40$, i.e. well past steady state.

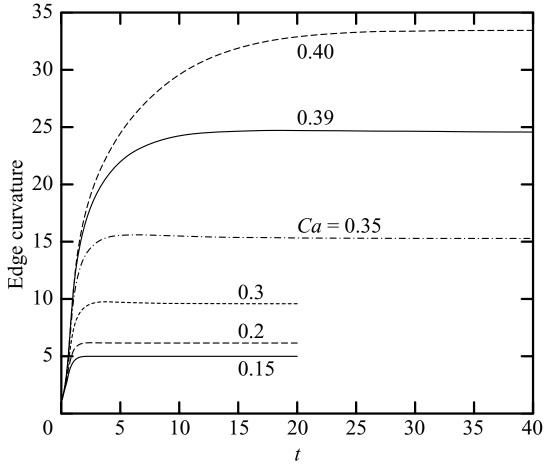

FIGURE 13. Time evolution of the edge curvature (determined along the interfacial cross-section with the $z = 0$ plane) for a neo-Hookean capsule with $\lambda = 1$ in a planar extensional flow with $Ca = 0.15, 0.2, 0.3, 0.35, 0.39, 0.4$.

the capsule's deformation D. The surface area of the capsule (not presented here) also shows a monotonic increase with time up to steady state and with flow rate similar to that of the capsule's length.

Figure 12(*a*, *b*) shows the evolution of the profile of a neo-Hookean capsule in the $z = 0$ and $y = 0$ planes for capillary number $Ca = 0.4$. Over time, the capsule elongates significantly in the flow direction and thins in the y-direction, while its depth shows a small increase. Thus the capsule shape at steady state is quite lamellar as shown in figure 12(*c*).

The evolution of the capsule profile with the plane $z = 0$, shown in figure 12(*a*), suggests that the edges of the neo-Hookean capsule become monotonically more pointed with time. This is shown clearly in figure 13 in which we have plotted the time evolution of the edge curvature for flow rates $Ca = 0.2, 0.3, 0.4$. The monotonic increase of the edge curvature is associated with the moderate hydrodynamic forces appearing at these flow rates as discussed above for the Skalak capsules. Figure 13

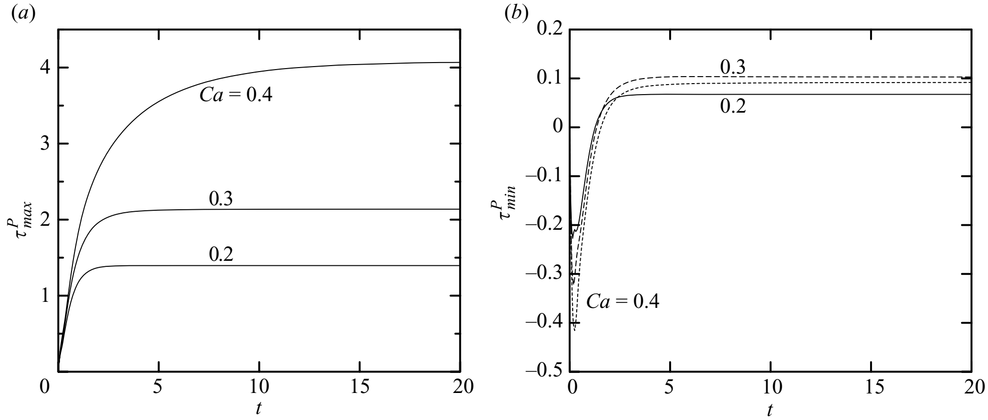

FIGURE 14. Time evolution of the (*a*) maximum τ^P_{max} and (*b*) minimum τ^P_{min} principal tensions among the spectral discretization points on the membrane for a neo-Hookean capsule with $\lambda = 1$ in a planar extensional flow with $Ca = 0.2, 0.3, 0.4$. (Note that for $Ca = 0.4$ our computations cover the time period [0, 40].)

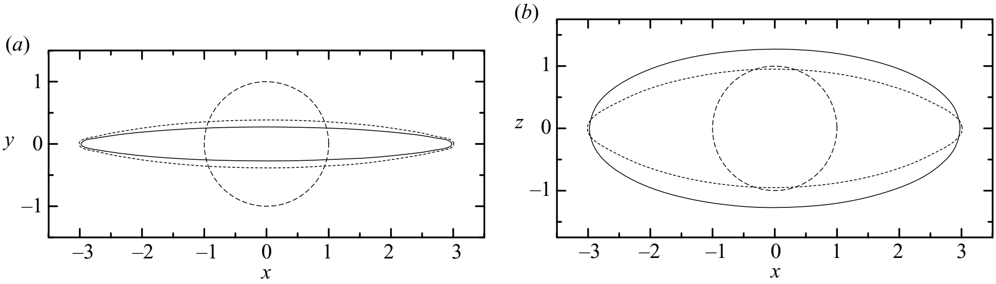

FIGURE 15. Steady-state profiles of a neo-Hookean capsule (——) for $Ca = 0.4$ and a Skalak capsule (- - - -) with $C = 1$ for $Ca = 2$ (which have similar extension), in a planar extensional flow with $\lambda = 1$. (*a*) Capsule profiles (i.e. interface intersections) with the plane $z = 0$. (*b*) As in (*a*) but for the capsule profiles with the plane $y = 0$. Also shown is the undisturbed profile (– –).

also reveals that at steady state, the edge curvature of the neo-Hookean capsule shows a rapid increase at high flow rates.

The time evolution of the maximum τ^P_{max} and minimum τ^P_{min} principal tensions over the surface of the neo-Hookean capsule is shown in figure 14. The maximum principal tension increases with time from a zero initial value until equilibrium; it is always positive, while higher flow rates cause larger values of τ^P_{max} at steady state. On the other hand, the minimum principal tension τ^P_{min} has a negative value at early times, while later it increases with time and becomes positive near steady state. The locations of the minimum and maximum tensions on the capsule surface follow the same trends as for the Skalak capsules described above. Since the membrane tensions at steady state are everywhere positive, no compression is developed, and thus the pointed edges of the neo-Hookean capsule are always concave as seen in figure 12.

Comparing the steady-state profiles of the neo-Hookean capsule for $Ca = 0.4$ and the Skalak capsule for $Ca = 2$ (which has similar length) it is obvious that the strain-softening capsule is thinner (i.e. it shows a smaller width S) and flatter (higher depth W) as seen in figure 15. Thus for the same extension L, the neo-Hookean capsule is more lamellar than the Skalak capsule.

It is of interest to note that the influence of the capillary number on the capsule's steady-state shape we present in this section is in qualitative agreement with the experimental findings included in the work of Barthès-Biesel (1991). As reported in figure 6 of Barthès-Biesel (1991), the steady-state shapes of polylysine membrane capsules in planar extensional flow show edges which are more rounded at small capillary numbers and become more pointed as Ca increases. (Note that we are not able to do quantitative comparisons, since the exact properties of the membrane in the experimental study are not known.)

As a summary, we have found that no critical flow rate exists for both Skalak and neo-Hookean capsules in the moderate and strong planar extension flows considered in the present study. At strong flows, both capsules reach elongated ellipsoidal steady-state configurations, while the neo-Hookean shapes are more lamellar than the Skalak ones for the same extension. The time evolution of the edge profiles are affected by the type of the experiment imposed on the capsule as well as the applied flow rate. Spherical capsules at moderate flow rates show a monotonic increase of the edge curvature up to steady state as found for capsules imposed to gradual flow rate increases even up to strong flows. On the other hand, when a spherical Skalak capsule is let to deform in a strong flow, the strong hydrodynamic forces overcome the initial weak membrane tensions, and thus initially the edge curvature increases trying to balance the hydrodynamic forces. After some time the membrane tensions increase (owing to the increased capsule deformation) and cause a decrease of the edge curvature towards its steady-state value. Thus, for the Skalak capsule in a strong flow rate, the maximum value of the edge curvature during the transient evolution can be several times its steady-state value.

In addition, our study reveals that the failure of earlier (low-order) computational methods at strong flow rates was a numerical artefact and not of physical origin as was reported (Lac *et al.* 2004). It is of interest to note that for both Skalak and neo-Hookean capsules, with or without prestress, in both shear and extensional flows, Lac *et al.* (2004) were able to determine interfacial deformation at steady state up to $D \approx 0.55$–0.6 (or for $L < 2$) as reported in table 1 of Lac *et al.* (2004) and figure 5 of Lac & Barthès-Biesel (2005). Our understanding is that this shows the upper numerical limit of the bi-cubic B-spline method of Lac *et al.* (2004), and thus it should not be confused as a physical phenomenon. In addition, we emphasize that the difficulty in the numerical computations is not only associated with the complicated interfacial shapes encountered in strong flows but also with the fact that for both Skalak and neo-Hookean membranes the elastic tensions are associated with nonlinear constitutive laws. (Note that the bi-cubic B-spline method of Lac *et al.* 2004 was able to determine elongated steady-state shapes for a capsule obeying the linear Navot law, as seen in figure 9 of Lac *et al.* 2004). With respect to this issue, our SBE method has the significant advantage of the accurate determination of any interfacial property as illustrated in § 4.

6. Steady-state properties of Skalak and neo-Hookean capsules in a planar extensional flow

In this section we present the steady-state properties of Skalak and neo-Hookean capsules in planar extensional flows as the flow rate increases. We consider both shape properties (i.e. the capsule lengths and the edge curvature) as well as the maximum tensions on the membrane (which can be used to predict rupture for a real membrane).

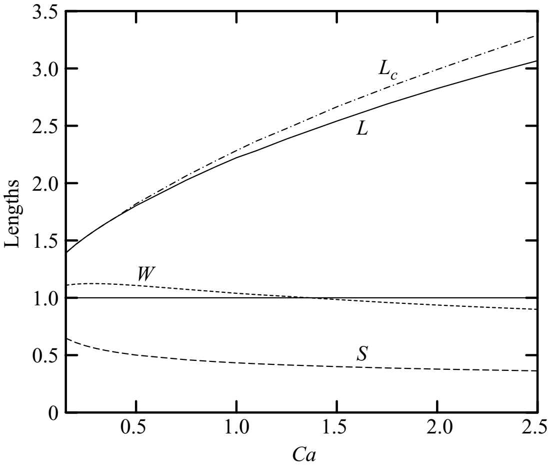

FIGURE 16. Steady-state half-lengths L, S and W (calculated from capsule's inertia tensor) as well as the capsule's actual half-length L_c as a function of the capillary number Ca for a Skalak capsule with $C=1$ and $\lambda=1$ in a planar extensional flow.

Our interest is mainly concentrated on the steady-state behaviour at high flow rates at which no information currently exists as discussed in § 1.

Figure 16 shows the half-lengths L, S and W of a Skalak capsule with $C=1$ as a function of the capillary number Ca. As the flow rate increases, the capsule length L is increased fast at first and then linearly at high flow rates. The capsule width S shows a slow monotonic decrease with the flow rate. On the other hand, the capsule depth W after an initial small increase decreases below its undisturbed value. It is of interest to note that Lac *et al.* (2004) predicted interfacial breaking for flow rates higher than an upper limit Ca_H, with $0.6 < Ca_H < 0.75$, and thus they reported the capsule's steady-state properties for $L < 2$ (see table 1 and figure 19 of Lac *et al.* 2004).

The flow rate dependence of the capsule's dimensions for the neo-Hookean membrane is shown in figure 17. Compared to the Skalak capsule, the length L of the neo-Hookean capsule increases faster with the flow rate, while its width S shows a fast decrease towards small values. Thus, owing to its strain-softening nature, the neo-Hookean capsule shows a much larger deformation for the same flow rate than that of the Skalak capsule. At the same time, the width W of the neo-Hookean capsule shows a monotonic increase which becomes quite rapid at large flow rates. Note that Lac *et al.* (2004) predicted interfacial breaking for flow rates higher than an upper limit Ca_H, where $0.21 < Ca_H < 0.24$, and thus they reported the capsule properties for $L < 1.75$.

At this point, it is of interest to note that the capsule dimensions, L, S and W presented in this paper, are determined as the semi-axes of the ellipsoid which has the same inertia tensor as that of the capsule (as discussed in § 4). For small and moderate deformations of an initially spherical shape, the corresponding lengths coincide with the actual capsule lengths. However, at large deformations results from the inertia tensor may under- or overestimate the true capsule dimensions, as we discussed in our earlier publication for large droplet deformations (see § 7 in Dimitrakopoulos 2007). As shown in figure 16, for a Skalak capsule the length L from the inertia tensor underestimates the actual half-length L_c of the capsule at large deformation;

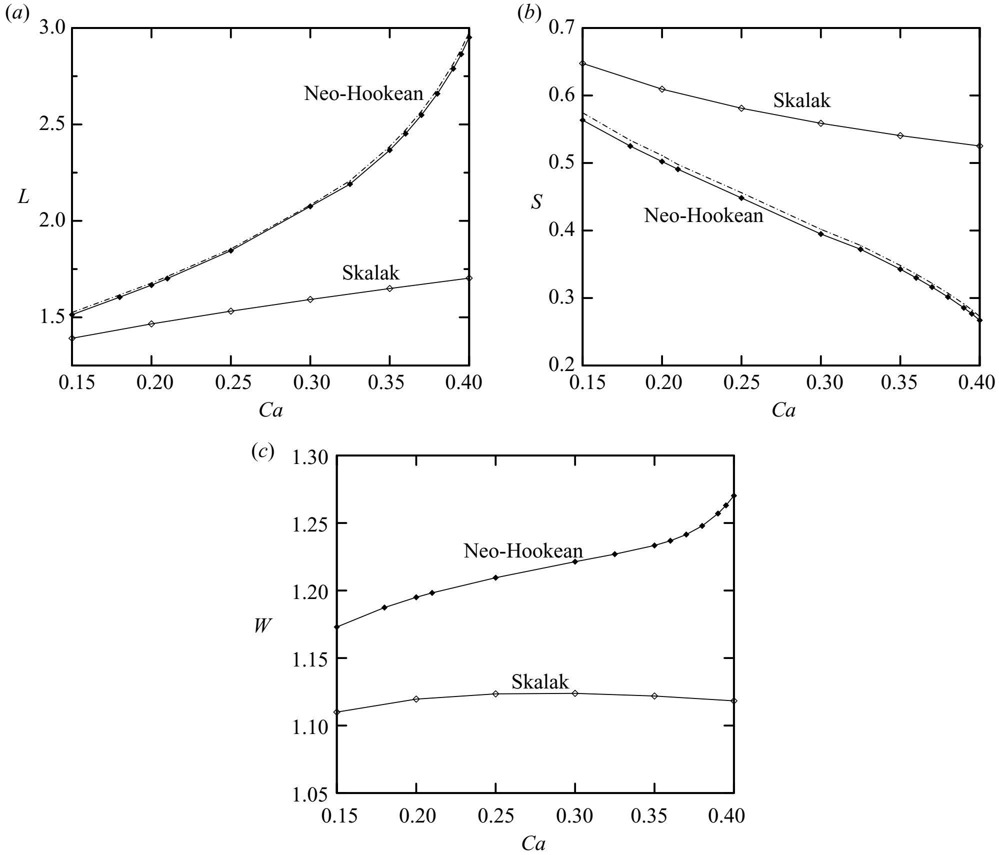

FIGURE 17. Steady-state half-lengths (calculated from capsule's inertia tensor) as well as the capsule's actual half-length L_c as a function of the capillary number *Ca* for a neo-Hookean capsule with $\lambda = 1$ in a planar extensional flow: (*a*) length *L*, (*b*) width *S* and (*c*) depth *W*. Note that in (*a*) and (*b*), the curves (–·–) denote the actual lengths, L_c and S_c, of the neo-Hookean capsule. Also shown are the lengths of a Skalak capsule with $C = 1$ for the same conditions.

however, *S* and *W* do measure the correct width S_c and depth W_c of the capsule for the range of capillary numbers presented in this paper. For a neo-Hookean capsule, figure 17 shows that only the width *S* underestimates slightly the actual width of the capsule. (Note that for any problem/type of flow, we calculate the actual semi-axes L_c and S_c as the maximum and minimum distance from the capsule's volume centroid to the interface by employing a Newton method for the optimization problems; for this problem W_c is easily determined via surface projection.)

We note that in § 5, we have presented the transient evolution of capsule lengths and the associated deformation *D* based on the inertia tensor so that we can compare our results with earlier studies which commonly determine the capsule dimensions from the inertia tensor. However, in our analysis in this section we will employ the actual capsule lengths which can easily be measured in any type of research, e.g. experiments.

Our results shown in figures 16 and 17 provide useful data and information for the behaviour of the two types of capsules with respect to the flow rate *Ca*. To illustrate more the effects of the extensional dynamics of the planar extensional flow on the

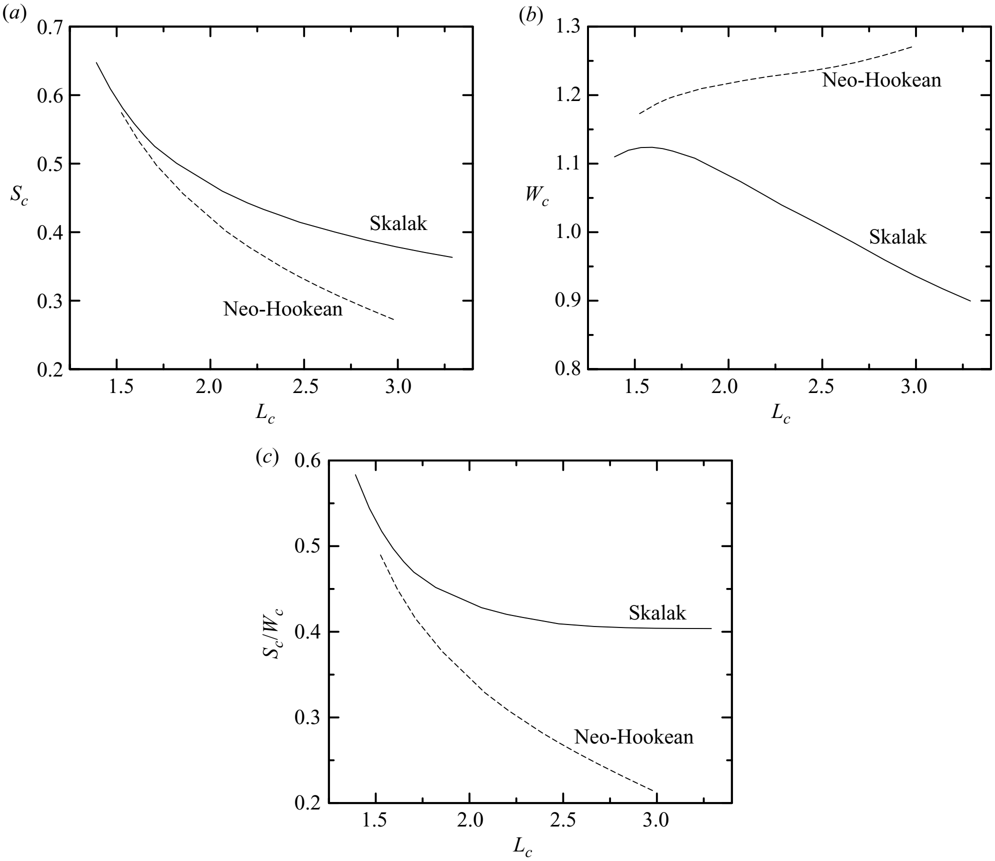

FIGURE 18. Steady-state capsule's dimensions as a function of its length L_c for a neo-Hookean and a Skalak capsule with $C = 1$ in a planar extensional flow: (*a*) width S_c, (*b*) depth W_c and (*c*) ratio S_c/W_c.

steady-state shape of the strain-hardening Skalak and strain-softening neo-Hookean capsules, in figure 18 we present the capsules' width and depth as function of their length L_c.

Figure 18 clearly shows that for the same extension L_c, the width of the neo-Hookean capsule decreases faster than that for the Skalak capsule. The evolution of the depth of the two types of capsule is quite different though; for a Skalak capsule the depth W_c decreases at high extensions, but the depth of neo-Hookean always increases. Thus, as we show in § 5, while both capsules obtain ellipsoidal-like shapes at high extensions, the strain-softening capsule is more lamellar. Figure 18(*c*) provides additional information on the cross-section of these capsules. At high extensions, the cross-section of the Skalak capsule preserves its length ratio S_c/W_c (i.e. it preserves its elliptical shape), while the neo-Hookean capsule becomes more and more lamellar with extension since its ratio S_c/W_c diminishes.

As shown in figure 19(*a*), the capsules' surface area S_B increases with the flow rate *Ca* in a manner similar to that for the capsule length L_c depicted earlier in figure 16. Therefore the surface area S_B shows a nearly linear increase with the capsule length L_c as seen in figure 19(*b*). It is of interest to note that for the same extension, the neo-Hookean capsule shows a greater surface area increase which can be attributed

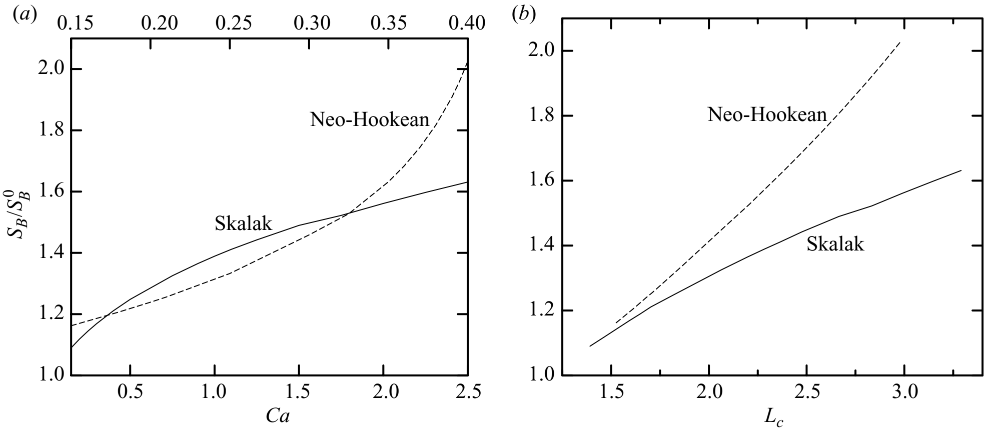

FIGURE 19. Surface area of the capsule at steady state S_B (scaled by the surface area S_B^0 of the reference spherical shape) as a function of (*a*) the capillary number Ca and (*b*) the capsule length L_c, for a neo-Hookean and a Skalak capsule with $C = 1$ in a planar extensional flow. Note that in (*a*) the neo-Hookean curve refers to the x-axis at the top of the figure.

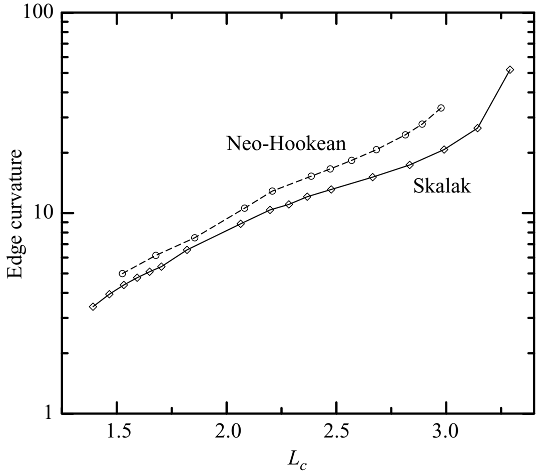

FIGURE 20. Steady-state edge curvature as a function of capsule's length L_c in a log-linear plot for a neo-Hookean and a Skalak capsule with $C = 1$ in a planar extensional flow.

to the its depth increase shown in figure 18(*b*). We note that in our work, the surface area of the neo-Hookean and Skalak capsules has been increased up to 102 % and 63 %, respectively. In this range of surface area increases, experimental findings have shown that the capsule dynamics can be well described by a single constitutive law with fixed value of the employed moduli, if an appropriate law for the membrane is used (e.g. see Carin *et al.* 2003). Thus our modelling is appropriate for real membranes for the entire range of deformations we study.

The capsules' profiles and shapes at steady state presented in § 5 demonstrate that at high flow rates, the large shape extensions result in the development of pointed edges with large curvature. To investigate this issue more, in figure 20 we plot the steady-state edge curvature (determined along the interfacial cross-section with the $z = 0$ plane) as a function of the capsule length for both types of membrane. As

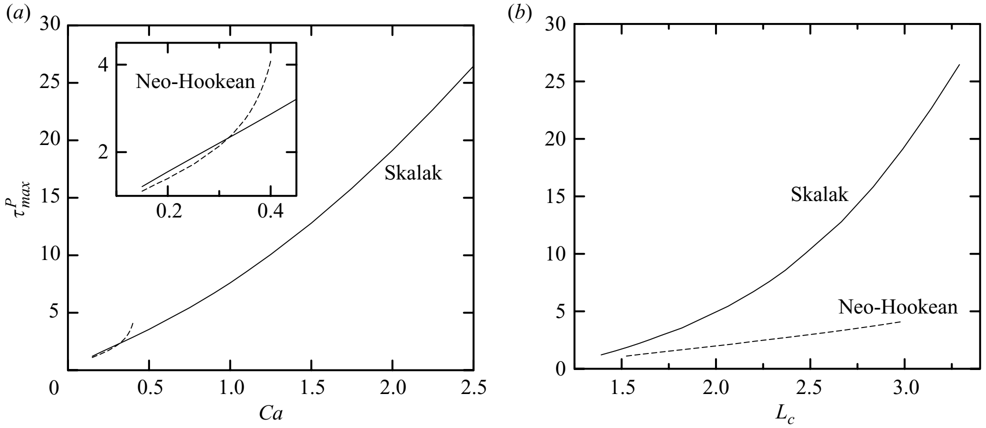

FIGURE 21. Steady-state maximum principal tensions τ^P_{max} among the spectral discretization points on the membrane as a function of (*a*) the capillary number *Ca* and (*b*) the capsule's length L_c, for a neo-Hookean and a Skalak capsule with $C = 1$ in a planar extensional flow. The inset in (*a*) shows the same variation for small capillary numbers.

the capsules' length increases, the curvature at the edges show a very fast increase especially at large lengths. In addition, the neo-Hookean capsule shows more pointed tips (i.e. higher edge curvature) at large extensions L_c; this may be attributed to the fact that its width decreases more than that of the Skalak capsule as seen in figures 15(*a*) and 18(*a*). It is of interest to note that figure 20 suggests that the edge curvature for both types of capsules follows an exponential-like increase with the capsule extension at steady state. (We note that owing to the relatively small range of the x-axis, it is not clear if the exponential-like increase shown in figure 20 is truly exponential; however, our results do show that the edge curvature increases at least as L_c^3.) The increase of the edge curvature with the flow rate at steady state is in agreement with published results for low-viscosity drops (e.g. Taylor 1934; Bentley & Leal 1986). Note that owing to the specific symmetry of the planar extensional flow, at steady state there is no flow inside the capsule; thus capsule dynamics at this flow type for any viscosity ratio corresponds better to the dynamics of low-viscosity drops.

We focus now our attention on the membrane tensions at steady state. Figure 21(*a*) reveals that on the surface of the Skalak capsule large tensions are developed which increase linearly with the flow rate *Ca* at strong flows. On the other hand, as shown in the inset of this figure, the maximum tensions on the neo-Hookean capsule show a late superlinear increase with the flow rate. The information presented in figure 21(*a*) can be used to predict the flow rate at which a specific membrane (with known lytic tension) will rupture due to excessive tensions in a planar extensional flow (assuming that the membrane elastic behaviour can be described by one of the two laws studied in this paper). As discussed in § 5 maximum tensions at steady state occur at the intersection of the capsule's surface with the z-axis; therefore this location is the most probable to rupture in an extensional flow.

In figure 21(*b*) we plot our data for the maximum principal tension τ^P_{max} as a function of the capsule's length L_c. As the capsule elongates in a planar extensional flow, the maximum tension on the neo-Hookean capsule increases nearly linearly, while that on the Skalak capsule shows a much faster increase with the capsule length. At the same extension L_c, owing to its strain-hardening nature the Skalak capsule shows much larger tensions than the strain-softening neo-Hookean capsule.

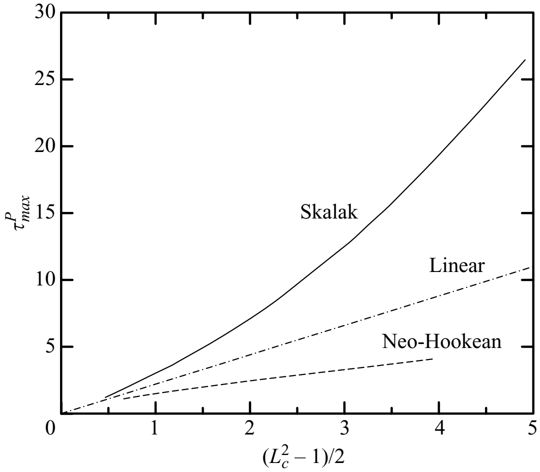

FIGURE 22. Steady-state maximum principal tension τ^P_{max} among the spectral discretization points on the membrane as a function of strain indicator $(L_c^2 - 1)/2$, where L_c is the capsule's length, for a neo-Hookean and a Skalak capsule with $C = 1$ in a planar extensional flow. The straight line (– · –) is an estimation of the initial common slope of the curves for the two capsules (based on our results for a Hookean capsule, e.g. see Barthès-Biesel *et al.* 2002) and denotes the linear growth of the tensions τ^P_{max} with the strain indicator $(L_c^2 - 1)/2$.

We conclude our investigation on the steady-state capsule behaviour, by considering how the tensions on the two types of capsules studied in this work increase with the applied strain. We note that the two principal strain components are connected with the principal stretch ratios λ_α by $(\lambda_\alpha^2 - 1)/2$ (see § 2.2 and Barthès-Biesel *et al.* 2002). Thus, assuming that the stretch ratio along the flow direction can be characterized by the capsule length L_c, the associated strain can be estimated as $(L_c^2 - 1)/2$. Figure 22 shows the maximum principal tensions τ^P_{max} for both capsules as a function of strain indicator $(L_c^2 - 1)/2$. This figure reveals the nature of the two types of membranes; the superlinear increase of the tensions on the Skalak capsule shows that this membrane is strain hardening. On the other hand, the sublinear increase of the tensions on the neo-Hookean capsule reveals its strain-softening nature. It is of interest to note that figure 22 is remarkably similar to figure 1 in Barthès-Biesel *et al.* (2002), where the tension versus strain relation was presented for several types of membranes undergoing (mechanically) uniaxial extension; this agrees with the main role of a planar extensional flow to produce elongation in the flow direction.

7. Conclusions

In the present study we have investigated via numerical computations the dynamics of initially spherical capsules (made from elastic membranes obeying the strain-hardening Skalak or the strain-softening neo-Hookean law) in strong planar extensional flows. In such flows current understanding of capsule dynamics is limited, since experimental findings are restricted to moderate flow rates; no asymptotic solutions exist, while the state-of-the-art (low-order) three-dimensional computational methodologies are unable to find stable steady-state capsule shapes.

To achieve our investigation, we have developed an SBE algorithm for interfacial dynamics in Stokes flow of three-dimensional capsules with shearing and area-dilatation tensions. To preserve the continuity of the interfacial geometry and its derivatives at the edges of the spectral elements during the interfacial deformation, a suitable interfacial smoothing based on a Hermitian-like interpolation has been developed which preserves the correspondence between the reference shape and the deformed geometry of the capsule. Our smoothing methodology, which we employ at every time step, applies to both the transient interfacial shape and the surface stress forces which depend on the membrane material.

Our interfacial SBE algorithm preserves the main characteristic of the spectral methods, i.e. high accuracy as the number of spectral points increases, but without creating denser systems as spectral methods used in volume discretization do. The accuracy of the method has been demonstrated for the calculation of the geometric properties of a given shape, such as the interfacial curvature, as well as the dynamic evolution of the interfacial shape. Our computational results for capsules obeying Skalak and neo-Hookean membrane laws in planar extensional flows at low and moderate capillary numbers are in agreement with those of earlier methodologies. However, at strong flow rates, our spectral algorithm is able to predict accurately stable transient and steady-state capsule shapes in contrast to earlier low-order methodologies which predict interfacial breaking owing to numerical instabilities.

In the current work we have investigated the capsule dynamics up to quite large deformations, i.e. surface area increases up to 102 % and 63 % for neo-Hookean and Skalak membranes, respectively. We emphasize that in this range of surface area increases, experimental findings have shown that the capsule dynamics can be well described by a single constitutive law with fixed value of the employed moduli (Carin *et al.* 2003), and thus our modelling is appropriate for the entire range of deformations we have studied.

Our computational investigation has revealed a number of new physical results and insight for the dynamics of strain-hardening Skalak and strain-softening neo-Hookean capsules at high flow rates which are commonly encountered in industrial and physiological processes.

In particular, at strong flows, both capsules reach elongated ellipsoidal steady-state configurations, but the neo-Hookean shapes are thinner and flatter (i.e. more lamellar) than the Skalak ones for the same extension. It is of interest to note that at high extensions, the cross-section of the Skalak capsule preserves its elliptical shape, while the neo-Hookean capsule becomes more and more lamellar with extension; thus for the same extension, the neo-Hookean capsule shows a larger surface area increase than that for the Skalak capsule. The large shape extensions result in the development of pointed edges with large curvature; our results suggest that the steady-state edge curvature for both types of capsules follows a very rapid increase with the capsule extension. The pointed profiles of these shapes are in qualitative agreement with experimental findings (Barthès-Biesel 1991). Thus our present work complements the similar evolution for low-viscosity drops which was first identified by the famous experiments of G. I. Taylor in 1934 (Taylor 1934), was further explained in the 1970s and 1980s (Buckmaster 1972; Acrivos & Lo 1978; Bentley & Leal 1986) and still finds useful applications (Ha & Leal 2001).

As the flow rate increases, the large interfacial deformations for both types of capsules are accompanied by the development of strong tensions especially for the strain-hardening Skalak capsule. Our findings on the increase of the membrane tensions with the flow rate or the shape extension (figure 21) can be used to predict the rupture of a specific membrane (with known lytic tension) due to excessive tensions in a planar extensional flow.

The type of the experiment imposed on the capsule as well as the applied flow rate affect dramatically the time evolution of the capsule edges owing to the interaction of the hydrodynamic forces with the membrane tensions. Spherical capsules at moderate flow rates show a monotonic increase of the edge curvature up to steady state as found for capsules imposed to gradual flow rate increases even up to strong flows. On the other hand, shortly after a spherical capsule is let to deform in a steady strong flow, the strong hydrodynamic forces overcome the weak membrane tensions; thus initially the edge curvature increases trying to balance the hydrodynamic forces. After some time the membrane tensions increase (owing to the increased capsule deformation) and cause a decrease of the edge curvature towards its steady-state value. Thus, for the Skalak capsule in a strong flow, very large edge curvatures (with respect to the steady-state value) can be developed during the transient evolution.

In addition, we have found that no critical flow rate exists for Skalak and neo-Hookean capsules in the moderate and strong planar extension flows considered in this study. The complicated interfacial shapes at high flow rates along with the fact that for both membrane types the elastic tensions are associated with nonlinear constitutive laws show that the failure of earlier computational methods at strong flow rates was a numerical artefact and not of physical origin owing to continuous interfacial extension as was reported by Lac *et al.* (2004).

It is of interest to note that $Ca = 0.4$ is the maximum flow rate at which we were able to compute accurate interfacial shapes for the neo-Hookean capsules; this flow rate corresponds to a very deformed lamellar interfacial shape with a semi-length $L \approx 3$ which is difficult to be computed numerically with the current version of our SBE method. (Note that in our computations we mainly used $N_E = 10, 14$ spectral elements; much denser grids were not employed owing to large computational cost.) However, our present results show no evidence of a critical flow rate for these capsules; e.g. observe the dependence of the capsule's length L and surface area S_B with the capillary number Ca presented in figures 17(a) and 19(a). For Skalak capsules, our interfacial spectral method is able to compute accurate shapes for flow rates up to $Ca = 3$ where $L \approx 3.6$, i.e. higher than those reported in the present study ($Ca \leqslant 2.5$). As discussed in our recent paper (Dodson & Dimitrakopoulos 2008), the strain-hardening capsules develop steady-state shapes whose edges from concave become cusped at sufficiently strong flow rates. The entire range of our results for Skalak capsules does not support the existence of a critical flow rate even for flows stronger than the ones considered in the present study. (See the dependence of the capsule's length L and surface area S_B with the capillary number Ca presented in figures 16 and 19a.) At this point, we need to emphasize that any computational methodology has an upper (numerical) limit, e.g. a very deformed interfacial shape above which the computational methodology breaks owing to numerical inability and numerical instabilities. However, one should be very careful in trying to associate a numerical breaking to a physical origin such as a critical flow rate.

We hope that our study serves as motivation for more experiments at high flow rates for both strain-hardening and strain-softening capsules. These experiments can be performed in classical or microfluidic four-roll mill devices (Ha & Leal 2001; Hudson *et al.* 2004). In such a case, the data for the capsule evolution and steady-state properties we have provided in this paper may help reveal how well certain membranes follow the neo-Hookean and Skalak constitutive laws at large deformations. It is of interest to note that the three-dimensional dynamics of the planar extensional flow helps to identify the true constitutive law valid for a given material.

The present algorithm constitutes a new approach for membrane deformation in Stokes flow based on the (high-order) SBE formulation which in the near past has demonstrated its high accuracy, robustness and efficiency for fixed boundary surfaces (Muldowney & Higdon 1995) and steady-state droplet interfaces under steady flows (Dimitrakopoulos & Higdon 1998) as well as for the transient droplet evolution (Wang & Dimitrakopoulos 2006; Dimitrakopoulos 2007). Owing to its spectral nature, our interfacial algorithm has the significant advantage of the accurate determination of any interfacial property, including geometric derivatives and membrane tensions. As discussed in § 5, we believe that this is an important issue for the correct and accurate determination of very deformed capsule shapes made from membranes obeying nonlinear elastic laws such as the Skalak and neo-Hookean (or Mooney–Rivlin) laws.

This work was supported in part by the National Science Foundation. Most computations were performed on multiprocessor computers provided by the National Center for Supercomputing Applications Applications (NCSA) in Illinois.

REFERENCES

Acrivos, A. & Lo, T. S. 1978 Deformation and breakup of a single slender drop in an extensional flow. *J. Fluid Mech.* **86**, 641–672.

Barthès-Biesel, D. 1980 Motion of a spherical microcapsule freely suspended in a linear shear flow. *J. Fluid Mech.* **100**, 831–853.

Barthès-Biesel, D. 1991 Role of interfacial properties on the motion and deformation of capsules in shear flow. *Physica* A **172**, 103–124.

Barthès-Biesel, D., Diaz, A. & Dhenin, E. 2002 Effect of constitutive laws for two-dimensional membranes on flow-induced capsule deformation. *J. Fluid Mech.* **460**, 211–222.

Barthès-Biesel, D. & Rallison, J. M. 1981 The time-dependent deformation of a capsule freely suspended in a linear shear flow. *J. Fluid Mech.* **113**, 251–267.

Barthès-Biesel, D. & Sgaier, H. 1985 Role of membrane viscosity in the orientation and deformation of a spherical capsule suspended in shear flow. *J. Fluid Mech.* **160**, 119–136.

Baskurt, O. K. & Meiselman, H. J. 2003 Blood rheology and hemodynamics. *Sem. Thromb. Hem.* **29**, 435–450.

Bentley, B. J. & Leal, L. G. 1986 An experimental investigation of drop deformation and breakup in steady, two-dimensional linear flows. *J. Fluid Mech.* **167**, 241–283.

Buckmaster, J. D. 1972 Pointed bubbles in slow viscous flow. *J. Fluid Mech.* **55**, 385–400.

Canuto, C., Hussaini, M. Y., Quarteroni, A. & Zang, T. A. 1998 *Spectral Methods in Fluid Dynamics.* Springer.

Carin, M., Barthès-Biesel, D., Edwards-Lévy, F., Postel, C. & Andrei, D. C. 2003 Compression of biocompatible liquid-filled HSA–alginate capsules: determination of the membrane mechanical properties. *Biotech. Bioengng* **82**, 207–212.

Chang, K. S. & Olbricht, W. L. 1993*a* Experimental studies of the deformation of a synthetic capsule in extensional flow. *J. Fluid Mech.* **250**, 587–608.

Chang, K. S. & Olbricht, W. L. 1993*b* Experimental studies of the deformation and breakup of a synthetic capsule in steady and unsteady simple shear flow. *J. Fluid Mech.* **250**, 609–633.

Diaz, A., Pelekasis, N. & Barthès-Biesel, D. 2000 Transient response of a capsule subjected to varying fluid conditions: effect of internal fluid viscosity and membrane elasticity. *Phys. Fluids* **12**, 948–957.

Dimitrakopoulos, P. 2007 Interfacial dynamics in Stokes flow via a three-dimensional fully-implicit interfacial spectral boundary element algorithm. *J. Comput. Phys.* **225**, 408–426.

Dimitrakopoulos, P. & Higdon, J. J. L. 1998 On the displacement of three-dimensional fluid droplets from solid surfaces in low-Reynolds-number shear flows. *J. Fluid Mech.* **377**, 189–222.

Dimitrakopoulos, P. & Wang, J. 2007 A spectral boundary element algorithm for interfacial dynamics in two-dimensional Stokes flow based on Hermitian interfacial smoothing. *Engng Anal. Bound. Elem.* **31**, 646–656.

Doddi, S. K. & Bagchi, P. 2008 Effect of inertia on the hydrodynamic interaction between two liquid capsules in simple shear flow. *Intl J. Multiphase Flow* **34**, 375–392.

Dodson, W. R., III & Dimitrakopoulos, P. 2008 Spindles, cusps and bifurcation for capsules in Stokes flow. *Phys. Rev. Lett.* **101**, 208102.

Eggleton, C. D. & Popel, A. S. 1998 Large deformation of red blood cell ghosts in simple shear flow. *Phys. Fluids* **10**, 1834–1845.

Gould, P. L. 1999 *Analysis of Shells and Plates.* Prentice Hall.

Ha, J. W. & Leal, L. G. 2001 An experimental study of drop deformation and breakup in extensional flow at high capillary number. *Phys. Fluids* **13**, 1568–1576.

Hudson, S. D., Phelan, F. R., Jr., Handler, M. D., Cabral, J. T., Migler, K. B. & Amis, E. J., 2004 Microfluidic analog of the four-roll mill. *Appl. Phys. Lett.* **85** (2), 335–337.

Husmann, M., Rehage, H., Dhenin, E. & Barthès-Biesel, D. 2005 Deformation and bursting of nonspherical polysiloxane microcapsules in a spinning-drop apparatus. *J. Colloid Interface Sci.* **282**, 109–119.

Kwak, S. & Pozrikidis, C. 2001 Effect of membrane bending stiffness on the axisymmetric deformation of capsules in uniaxial extensional flow. *Phys. Fluids* **13**, 1234–1242.

Lac, E. & Barthès-Biesel, D., 2005 Deformation of a capsule in simple shear flow: effect of membrane prestress. *Phys. Fluids* **17**, 072105.

Lac, E., Barthès-Biesel, D., Pelekasis, N. A., & Tsamopoulos, J. 2004 Spherical capsules in three-dimensional unbounded Stokes flows: effect of the membrane constitutive law and onset of buckling. *J. Fluid Mech.* **516**, 303–334.

Lubarda, V. A. 2002 *Elastoplasticity Theory.* CRC Press.

Mohandas, N. & Chasis, J. A. 1993 Red blood cell deformability, membrane material properties and shape: regulation by transmembrane, skeletal and cytosolic proteins and lipids. *Sem. Hematol.* **30**, 171–192.

Muldowney, G. P. & Higdon, J. J. L. 1995 A spectral boundary element approach to three-dimensional Stokes flow. *J. Fluid Mech.* **298**, 167–192.

Navot, Y. 1998 Elastic membranes in viscous shear flow. *Phys. Fluids* **10**, 1819–1833.

Papastavridis, J. G. 1999 *Tensor Calculus and Analytical Dynamics.* CRC Press.

Pieper, G., Rehage, H. & Barthès-Biesel, D. 1998 Deformation of a capsule in a spinning drop apparatus. *J. Colloid Interface Sci.* **202**, 293–300.

Popel, A. S. & Johnson, P. C. 2005 Microcirculation and hemorheology. *Annu. Rev. Fluid Mech.* **37**, 43–69.

Pozrikidis, C. 1995 Finite deformation of liquid capsules enclosed by elastic membranes in simple shear flow. *J. Fluid Mech.* **297**, 123–152.

Pozrikidis, C. 2001 Effect of membrane bending stiffness on the deformation of capsules in simple shear flow. *J. Fluid Mech.* **440**, 269–291.

Pozrikidis, C. 2001 Interfacial dynamics for Stokes flow. *J. Comput. Phys.* **169**, 250–301.

Pozrikidis, C. (Ed.) 2003 *Modelling and Simulation of Capsules and Biological Cells.* Chapman and Hall.

Ramanujan, S. & Pozrikidis, C. 1998 Deformation of liquid capsules enclosed by elastic membranes in simple shear flow: large deformations and the effect of fluid viscosities. *J. Fluid Mech.* **361**, 117–143.

Secomb, T. W., Hsu, R. & Pries, A. R. 1998 A model for red blood cell motion in glycocalyx-lined capillaries. *Am. J. Physiol. Heart Circ. Physiol.* **274**, H1016–H1022.

Secomb, T. W., Hsu, R. & Pries, A. R. 2001 Motion of red blood cells in a capillary with an endothelial surface layer: effect of flow velocity. *Am. J. Physiol. Heart Circ. Physiol.* **281**, H629–H636.

Secomb, T. W., Hsu, R. & Pries, A. R. 2002 Blood flow and red blood cell deformation in non-uniform capillaries: effects of the endothelial surface layer. *Microcirculation* **9**, 189–196.

Skalak, R., Tozeren, A., Zarda, R. P. & Chien, S. 1973 Strain energy function of red blood cell membranes. *Biophys. J.* **13**, 245–264.

Steigmann, D. J. & Ogden, R. W. 1999 Elastic surface-substrate interactions. *Proc. R. Soc. Lond.* A **455**, 437–474.

Taylor, G. I. 1934 The formation of emulsions in definable fields of flow. *Proc. R. Soc.* A **146**, 501–523.

Wang, Y. & Dimitrakopoulos, P. 2006 A three-dimensional spectral boundary element algorithm for interfacial dynamics in Stokes flow. *Phys. Fluids* **18**, 082106.

Waxman, A. M. 1984 Dynamics of a couple-stress fluid membrane. *Stud. Appl. Math.* **70**, 63–86.